Mesoscopic-Scale Complexity in Macroscopically-Uniform Plastic Flow of an Al0.3CoCrFeNi High-Entropy Alloy

Jamieson Brechtl, Rui Feng, Peter K Liaw, Benoît Beausir, Hafsa Jaber, Tatiana Lebedkina, M.A. Lebyodkin

Mesoscopic-Scale Complexity in Macroscopically-Uniform Plastic Flow of an $Al_{0.3}CoCrFeNi$ High-Entropy Alloy

Jamieson Brechtl[1,*], Rui Feng[2], Peter K. Liaw[1,*], Benoît Beausir[3], Hafsa Jaber[3], Tatiana Lebedkina[3,4], and Mikhail Lebyodkin[3]

[1]The University of Tennessee, Knoxville, TN 37996, USA

[2]Oak Ridge National Laboratory, Oak Ridge, TN 37831, USA

[3]Laboratoire d'Etude des Microstructures et de Mécanique des Matériaux (LEM3), CNRS, Université de Lorraine, Arts & Métiers ParisTech, 7 rue Félix Savart, 57070 Metz, France;

[4]Center of Excellence "LabEx DAMAS", Université de Lorraine, 7 rue Félix Savart, 57070 Metz, France

[*] Corresponding author. Email: jbrechtl@vols.utk.edu ; pliaw@utk.edu

Abstract

The concept of a smooth and homogeneous plastic flow of solids is nowadays constantly challenged by various observations of the self-organization of crystal defects on mesoscopic scales pertaining, e.g., to acoustic emission or the evolution of the local strain field. Such investigations would be of particular interest for High-Entropy Alloys (HEAs) characterized by extremely complex microstructures. However, the complexity of their deformation has been only studied in relation to the jerky flow. The present work explores a mesoscale complexity of the macroscopically-smooth plastic flow of an $Al_{0.3}CoCrFeNi$ alloy. An inclusive approach involving various experimental methods and complementary nonlinear analyses allowed to reveal transitions between distinct dynamical regimes, which may be assimilated with noises of different colors, in particular the blue noise that is rarely observed in complex systems, and various kinds of reddened behavior. Such findings provide significant new insights into the micro/macro transition in the deformation behavior of HEAs.

Keywords: High-entropy alloys; Scale transitions; Digital image correlation; Acoustic emission; Statistical analysis

1. Introduction

High-entropy alloys (HEAs) are a relatively-newer class of materials that have garnered attention for almost two decades [1,2]. HEAs usually consist of five or more principal elements each comprising roughly 5 to 35 atomic percent (at. %) of the alloy [3,4]. Such a combination results in a high mixing entropy that favors disordered solid solutions at elevated temperatures [5]. These types of alloys have been reported to exhibit attractive properties, such as biocompatibility [6,7], excellent corrosion resistance [8], irradiation resistance [9–11], excellent wear resistance [12,13], good fatigue resistance [14–16], great strength and fracture toughness [17–20], high ductility [21–23], and suitable cryogenic tensile and fracture properties [21,24,25].

High-entropy alloys are often subject to jerky flow [26,27]. Regardless of the specific mechanisms and manifestations of this phenomenon, this behavior unifies the nonlinear physics of their plastic flow with various metals and alloys. Abundant literature evidenced that jerky flow can exhibit a complexity that is associated with scale invariance [28,29]. Such fluctuations have been observed in a variety of metal systems, including single and polycrystalline metals [30], steels [26,31,32], Al alloys [26,28,33], Cu alloys [34], V alloys [35], bulk-metallic glasses (BMGs) [26,36,37], and medium entropy- and high-entropy alloys [27,38–42]. The observation of complexity implies that the fundamental understanding of macroscopic behavior cannot be deduced from the averaging of the supposedly stochastic microscopic dynamics of individual dislocations, but the self-organization resulting from their interaction must be considered. Lately investigations on conventional materials showed that a mesoscopic-scale range is the main scene for the phenomena caused by the self-organization of dislocations [43–53] . Significant efforts to link the macroscopic and microscopic behavior were based on the analysis of the statistics of the acoustic emission (AE) accompanying the plastic flow of various materials, both during

macroscopically-smooth deformation (e.g., [43,44]) and during jerky flow (e.g., [45–47]). It was found that deformation processes are inherently avalanche in nature in the relevant scale range. However, this conception does not help yet establish the link between such universal dynamics pertaining to the AE and the variety of macroscopic behaviors. Another intermediate-scale range may be uncovered by the optical extensometry techniques, e.g., the digital image correlation (DIC) [54]. This range has been little explored from the viewpoint of the self-organization [43,50,52,53]. Therewith, investigations of mesoscopic-scale collective dislocation effects in the HEAs have not been undertaken so far, because of the recency of this material.

The purpose of the paper is to investigate this missing link by studying the fine-scale heterogeneity of deformation processes during the macroscopically-smooth plastic flow of a HEA alloy. The salient feature of the undertaken research is a comprehensive approach, which includes various kinds of experiments and data analyses aimed at the quantification of the complexity that may be hidden in the small fluctuations on deformation curves, DIC, or AE. As these novel alloys with highly-complex microstructures are an outstanding example of complex behaviors in natural dynamical systems, these results will shed light on the general questions, concerning not only HEAs but any materials, of the interplay between the strain fields and the underlying dynamical behavior at mesoscopic scales, and of the relationship between meso- and macroscale behaviors.

2. Materials and Methods

2.1 Material

The $Al_{0.3}CoCrFeNi$ HEA used for experiments was similar to that studied in [55] which describes its microstructure in detail. The material with a nominal chemical composition of 7.00Al23.26Co-23.26Cr-23.26Fe-23.26Ni (at.%) was fabricated by vacuum-induction melting to a plate (~ 127 mm × 305 mm × 19 mm). Then the hot-isostatic-pressing process at 1,204 °C and

103 MPa was employed to the plate for 4 hours. After that, the specimens were homogenized at 1,250 °C for 2 hours, followed by water quenching. This combination of the chemical composition and processing allowed to obtain an almost single solid-solution face-centered-cubic (*fcc*) phase. The resulting mean grain size was larger than 600 μm, with the greatest diameter up to about 1.5 mm. Commonly two to four grains appeared across the specimen thickness (up to about fifty grains over the gauge length), as can be seen in Fig. A1 of the appendix. Besides, the material had many twins [examples of twins can be recognized in Figs. A1 (c) and (d); see [55] for more detail].

2.2 Mechanical Testing

The $Al_{0.3}CoCrFeNi$ HEA samples underwent room-temperature tension testing in a screw-driven machine Zwick/Roell 1476 at the nominal strain rate, $\dot{\varepsilon}_a$, ranging from 10^{-6} to 10^{-3} s^{-1}. Samples had a dog-bone shape with the gage linear dimensions of 35 × 6.98 × 1.54 mm. The load cell of the deformation machine had a resolution of 0.06 N. The sampling time was equal to 10 ms at the highest $\dot{\varepsilon}_a$ value and was proportionally increased when $\dot{\varepsilon}_a$ was decreased. In the latter cases, several intervals were recorded with shorter sampling times (down to 4 ms) in order to verify that significant information was not smoothed out upon coarsening the time resolution.

2.3 Data Analysis

2.3.1 Digital-Image Correlation

The local strain-rate field was evaluated, using the method of DIC, as described in detail in [54]. For this process, a black-and-white speckle pattern was painted on one specimen surface, and its displacement was followed by a Charged-Coupled Device camera, which provided a spatial resolution of 25 μm/pixel. Local strains in the tensile direction were reconstructed from the difference between the current and the initial (reference) images with the aid of the standard image correlation software, VIC-2D [56], using a subset size of 21 pixels and a spacing of 5 pixels. The

spatial resolution of strain approximately corresponded to a window with a 150 μm side. The numerical derivation of the local strain field with regard to time allowed to calculate the strain-rate field and visualize the evolution of the heterogeneity of the plastic activity. Besides the assessment of two-dimensional (2D) local strain-rate patterns at selected instants, the successive series of such images were used to construct spatiotemporal maps visualizing the evolution of the local strain rate along a selected cross-section of the sample as a function of time.

The images were recorded at a rate of 1 frame per 65 ms in the fastest tests. When $\dot{\varepsilon}_a$ was reduced, the acquisition frequency was reduced to gather data during the entire test duration. In this case, several intervals corresponding to various deformation stages were recorded with the highest time resolution.

2.3.2 Acoustic Emission (AE)

AE allows for further increasing both the time resolution and the sensitivity of the measurements to the collective motions of dislocations. The approach to the AE analysis was deliberately chosen similar to that used previously in the investigations of jerky flow in conventional alloys [45,57], so that to provide a basis for the comparison of the results of the corresponding statistical analyses without possibly biasing the recorded data. The signal from a piezoelectric transducer (frequency band of 200 – 900 kHz) clamped to the greased surface of the specimen near the upper grip was pre-amplified by 40 dB and registered at a frequency of 2 MHz using a Euro Physical Acoustic system [58]. The signal contains a continuous component and discrete spikes [47] that are generally ascribed to the motion of large groups of dislocations and are tantamount to the avalanche-like dynamics of the dislocation system. Such discrete events (hits) were extracted in the real time with the aid of several preset parameters, namely, a threshold voltage, U_o (25 dB in the present study), usually taken just above the noise level, and two time

parameters. More specifically, while the event's starting time is identified in an obvious way when the acoustic signal exceeds the threshold, the identification of its end is less evident. It is considered to terminate if after this instant, the signal remains below the threshold longer than for a hit definition time (HDT). Also, a hit lockout time (HLT) during which the system finds itself in an idle mode is imposed to filter out reverberations after the end of the hit. Finally, a peak definition time (PDT) is used to determine the hit's amplitude. Namely, the current local maximum of the signal is recorded as the peak amplitude if it has not been exceeded during PDT. In the present work, the time parameters were chosen as follows: {HDT,HLT,PDT} = {50 μs, 100 μs, 40 μs}. It is noteworthy that such a hit-based approach exploits only a part of information contained in the continuously recorded AE signal (cf., e.g., [59,60] for the so-called data-streaming approach). The analysis of the latter goes beyond the scope of the present paper and will be published elsewhere.

2.4 Mathematical Analysis

To unmask the order hidden in the measured signals may require various complimentary approaches because it can manifest itself in various characteristics highlighting distinct features of the signal. The methods used included the Fourier spectral analysis, evaluation of statistical distributions of the signal fluctuations, entropy-based analysis, and estimation of fractal dimensions with the aide of the multifractal (MF) and rescaled range (R/S) techniques. The last three methods are recalled below. It is important to specify that the analyses were applied to detrended signals, i.e., obtained after removal of the average trend caused by the work hardening, within time intervals where the fluctuations of the processed signal demonstrated a stationary character. As a quantitative control, it was also checked that the results of the anaysis were robust when the interval length was varied keeping a sufficient number of data points (see, e.g., [27,28]).

2.4.1 Refined Composite Multiscale Entropy (RCMSE) Analysis

For the refined composite multiscale entropy (RCMSE) analysis, the basic procedure from [61] was used. As a first step, a moving average or a third order polynomial is used to fit the stress vs. time data (a strain-hardening regime) and remove the underlying trend [28,33,62]. The coarse-grained time series is then created from the resulting data:

$$y_{k,j}^{\tau} = \frac{1}{\tau} \sum_{i=(j-1)\tau+k}^{j\tau+k-1} x_i \quad ; \; 1 \leq j \leq \frac{N}{\tau} \qquad 1 \leq k \leq \tau \tag{1}$$

here N and x_i are the total number of data points and the *ith* point of the detrended time-series data, respectively, τ is the scale factor, and k is an indexing factor, which designates where in the series to begin the coarse-graining. Next, create the template vector, $y_{k,i}^{\tau,m}$, of a dimension, m:

$$\boldsymbol{y_{k,i}^{\tau,m}} = \left\{ y_{k,i}^{\tau} \;\; y_{k,i+1}^{\tau} \;\ldots\; y_{k,i+m-1}^{\tau} \right\} \;\; ; \quad 1 \leq i \leq N-m \,; 1 \leq k \leq \tau \tag{2}$$

where $y_{k,j}^{\tau}$ is calculated, using Eq. (1). Now evaluate the *kth* template vectors of a dimension, m:

$$\boldsymbol{y_k^{\tau}} = \left[\boldsymbol{y_{k,1}^{\tau}} \;\; \boldsymbol{y_{k,2}^{\tau}} \;\; \ldots \;\; \boldsymbol{y_{k,i+m-1}^{\tau}} \right] \tag{3}$$

Next find n-matching sets of distinct template vectors for each k, using the following equation:

$$d_{jl}^{\tau,m} = \left\| \boldsymbol{y_j^{\tau,m}} - \boldsymbol{y_l^{\tau,m}} \right\|_{\infty} = \max\left\{ \left| y_{1,j}^{\tau} - y_{1,l}^{\tau} \right| \ldots \left| y_{i+m-1,j}^{\tau} - y_{i+m-1,l}^{\tau} \right| \right\} < r \tag{4}$$

here $d_{jl}^{\tau,m}$ is the uniform norm, and r is a limiting factor. The value, r, is typically chosen as 0.15 times of the standard deviation of the data [3] to ensure that the sample entropy is independent of the variance of the data [63,64]. Two vectors match when the norm is less than r. After this

procedure is completed for m, it is repeated for vectors of a size, $m + 1$. From the results, the total number of matching vectors, $n_{k,\tau}^{m}$, for m and $m + 1$ can be evaluated by summing from $k = 1$ to τ. This result is then used to compute the RCMSE (or sample entropy) value for the detrended time-series data:

$$RCMSE(\boldsymbol{X}, \tau, m, r) = Ln\left(\frac{\sum_{k=1}^{\tau} n_{k,\tau}^{m}}{\sum_{k=1}^{\tau} n_{k,\tau}^{m+1}}\right) \quad (5)$$

Another important metric is the complexity index (*CI*), which is simply the average value of the RCMSE function with respect to the scale factor [65]:

$$CI = \frac{1}{\tau_{max} - \tau_{min}} \int_{\tau_{min}}^{\tau_{max}} RCMSE(\boldsymbol{X}, \tau, m, r) d\tau \quad (6)$$

where τ_{max} and τ_{max} equal 1 and 20, respectively.

2.4.2 Multifractal and R/S analyses

The underlying concepts and various approaches of the mathematical description of the MF formalism may be found in numerous books (e.g., [66]). Like in the case of the RCMSE analysis, the practical application to stress-time curves starts with the removal of the regular trends caused by the work hardening of the material [28,33,67]. Similar procedures are applied in the present work to both stress and local strain-rate signals. Below are presented some basic formulae necessary for the understanding of the results of the MF analysis of these signals.

The signal measured in a computer-assisted experiment is represented by a discrete time series, ψ_k, where k enumerates the data points. In order to test scaling properties of the signal, the analyzed time interval is covered by a grid with a step, δt, and a local probabilistic measure, $\mu_i(\delta t)$, is defined to characterize its value in the ith time interval. Two definitions of μ were probed

in the present work. The first one adapts the approach proposed for the analysis of a jerky flow [28,33,67]. This formalism defines the local measure for the *i*th time box as the sum of the absolute values of the finite difference approximant of the signal within the box, normalized by the sum over all *N* boxes. In the case of the deformation curve, this definition is well adapted to signals dominated by bursts associated with jerky flow. The second definition considers the normalized spread of the signal within the *i*th box:

$$\mu_i(\delta t) = \frac{(\psi_{max} - \psi_{min})_i}{\sum_N (\psi_{max} - \psi_{min})_i} \tag{7}$$

The results obtained in the two cases were compatible, but the second definition occurred to be better adapted to the analysis of fluctuating signals without (or with a small number) of spikes. The self-similarity is then assessed by investigating the scaling of the families of partition functions corresponding to different values of the order, q:

$$Z_q(\delta t) = \sum_i^N \mu_i^q(\delta t), q \neq 1\,;\; Z_1(\delta t) = \sum_i^N \mu_i(\delta t) ln \mu_i(\delta t), q = 1 \tag{8}$$

Herewith, the variation of q makes dominate different μ values in $Z_q(\delta t)$ and, therefore, allows to probe the scaling for distinct data subsets assembling boxes with similar values of the local measure. In the case of a MF signal, the partition functions obey a scaling law in the limit, $\delta t \to 0$:

$$Z_q(\delta t) = \delta t^{(q-1)D_q},\ q \neq 1;\ Z_1(\delta t) = D(1)\ln(\delta t)\,, q = 1 \tag{9}$$

where D_q denotes the generalized fractal dimensions. In the case of real signals, these relationships are satisfied in bounded ranges of δt because experimental data possess characteristic scales, e.g., implied by the experimental noise at small scales or, in the opposite limit, by the system size.

To relate this description to the well-known notion of the fractal dimension, it may be specified that taking $q = 0$ corresponds to the box-counting method of calculations of the fractal dimension of the geometrical support of the signal, i.e., counting the boxes containing a non-zero value of the measure. In the present case, D_0 is close to the trivial case ($D_0 = 1$) because the signal is nonzero almost everywhere along the time axis.

In what follows, a more intuitively-clear representation is used instead of the generalized dimension, $D(q)$, the so-called singularity spectra, $f(\alpha)$, which makes use of the scaling of the self-similar measure with regard to the box size [66,68]:

$$\mu_i(\delta t) \sim \delta t^{\alpha} \tag{10}$$

where α denotes the singularity strength of the local measure. The corresponding f-value gives the fractal dimension of the subset of boxes corresponding to the singularity strength in the vicinity of α. In other words, $f(\alpha)$ describes the heterogeneous object as interpenetrating fractal subsets. Both kinds of descriptions are related via the Legendre transformation [28], so that the singularity "spectrum" may be deduced from the "spectrum" of generalized dimensions. In the present study, we use a direct method of calculating $f(\alpha)$ suggested in [69] and based on scaling relationships for a normalized measure, $\tilde{\mu}_i(\delta t, q) = \mu_i^q / \sum_j \mu_j^q$:

$$\begin{aligned} \Sigma_\alpha(\delta t, q) &= \textstyle\sum_i \tilde{\mu}_i\,(\delta t, q)\; ln\, \mu_i\,(\delta t) \sim \alpha(q) ln \delta t \\ \Sigma_f(\delta t, q) &= \textstyle\sum_i \tilde{\mu}_i\,(\delta t, q) ln \tilde{\mu}_i(\delta t, q) \sim f(q)\; ln\; \delta t \end{aligned} \tag{11}$$

Another convenient way to uncover self-similarity in a fractal time series is based on the R/S method which examines the scaling of the range, $R(\tau)$, of the cumulated deviations of the time series, ψ_k, from its average $< \psi >_\tau$ over a given time interval, τ [66]. $R(\tau)$ is found as:

$$R(\tau) = X(t, \tau)_{max} - X(t, \tau)_{min} \tag{12}$$

where the cumulated deviation at a (discrete) instant, $1 \leq t \leq \tau$, is calculated as:

$$X(t,\tau) = \sum_{k}^{t} (\psi_k - < \psi >_\tau) \tag{13}$$

For a fractal time series, the following scaling relation is fulfilled:

$$R/S \sim \tau^H \tag{14}$$

where S is the standard deviation of ψ_k over τ. The Hurst exponent, H, is related via a simple relationship to the fractal dimension, D, of the curve traced by the time series in a 2D space: $D = 2 - H$. This exponent is often used to characterize the generalized Brownian noise. The value of $H = 1/2$, which corresponds to the classical random process with independent increments, separates the ranges of H values corresponding to a qualitatively different nature of correlations within the signal. For $H < 1/2$, the dynamics can be characterized by anti-persistent behavior, where an increase in the signal implies a tendency to its further decrease, while the tendency is opposite for persistent behavior for $H > 1/2$.

3. Results

3.1 Deformation curves and DIC patterns

Figure 1 displays an example of the stress-time data and the corresponding spatiotemporal map for the sample tested at an imposed strain rate, $\dot{\varepsilon}_a = 10^{-3}$ s^{-1}. Deformation curves demonstrated a similar shape for all $\dot{\varepsilon}_a$, namely, three-stage behavior with a convex part after an elastoplastic transition, i.e., the work hardening was initially low, increased after some deformation, then decreased again towards the onset of necking. As illustrated in Fig. 1(a), they do not display serrations. In consistence with their smoothness, the comparison of the deformation curves

recorded at different $\dot{\varepsilon}_a$ revealed a positive strain-rate sensitivity of stress (SRS). It is worth recalling that the jerky flow is associated with negative SRS values [29].

The evolution of the strain localization can be observed in the spatiotemporal map from Fig. 1(b), which represents data on the local strain rate, $d\varepsilon_{loc}/dt$, collected along the vertical centerline (the tensile axis) of the specimen. Although the deformation curves are macroscopically smooth, the DIC reveals deformation heterogeneity on a finer scale. Namely, the local activity does not cover the map uniformly, but shows a tendency to localize at some sections. In the example of Fig. 1, mainly two large regions of localized plastic flow are formed during the elastoplastic transition, about 3 and 9 mm wide, i.e., covering several grains. The localization becomes weaker (decays into multiple zones) after the inflection point on the deformation curves, when the work-hardening rate starts increasing. This stage corresponds to a stabilized signal with a stationary range of fluctuations of the local strain rate. In the present work, the mathematical analysis presented below (see Sec. 3.3) was performed in strain intervals chosen within this period of stabilized behavior.

Figure 2 displays a series of 2D DIC images corresponding to the map of Fig. 1(b). The first image illustrates that the deformation is rather uniform before the elastoplastic transition. The next frames highlight the formation of several places where deformation tends to localize subsequently. Indeed, the maximum local strain rate in the red regions is about 3 times higher than $\dot{\varepsilon}_a$. The images before 27 s show the first localization zone formed at the elastoplastic transition. Then another zone appears at the center of the gage length. The strain field gradually becomes more homogeneous due to the occurrence of multiple zones of localization. The concurrence between the localization and the homogenization is consistent with the wavy final shape of the specimen in the last image where a large red region unveils the ultimate neck.

Importantly, the images from Fig. 2 show that the regions of the maximum local strain rate within the zones of strain localization detected on the strain-rate map of Fig. 1(b) correspond to shear bands. The shear-band geometry has been observed for the jerky flow in various materials, including conventional alloys and BMGs [54,70]. That is, although the bands found in the present work are rather weak, they have a geometry similar to that of the bands associated with the jerky flow. In the studied HEA alloy, the bands often appear quasi-instantaneously through the entire cross-section, according to one of the known scenario of the deformation-band formation [71,72]. Furthermore, the strain localization may occur in unconnected isles (frames 2, 3, 6, and 7 that correspond, respectively, to times of 20.74 s, 21.46 s, 47.14 s, and 104.3 s), which then percolate and form a complete deformation band across the specimen width. The size of such isles corresponds to the average grain size, which bears evidence that each nucleus of the nascent deformation band develops within one grain. At the same time, the nuclei appear in a correlated manner in several sites corersponding to different grains, so that the emerging pattern follows a shear-band orientation from the onset of the band development. This direct manifestation of the correlation of deformation processes underlines the need of the analysis of various responses of the material to plastic flow, undertaken in the following sections.

3.2 Analysis of force signals

Figures 3(a)-(b) present the detrended force vs. time signals, $F(t)$, for samples tested at strain rates of 10^{-3} s^{-1} and 10^{-5} s^{-1}, respectively. It can be recognized that after the subtraction of the systematic trend governed by the work hardening, the deformation curves exhibit small fluctuations. It is natural to suggest that they are related to the heterogeneous and non-stationary plastic activity visualized in Figs. 1 and 2. Even before performing a quantitative analysis, it can be concluded that two signals corresponding to various $\dot{\varepsilon}_a$ are strongly different. The signal

obtained at the highest $\dot{\varepsilon}_a$ consists of multiperiodic oscillations [Fig. 3(a)], while more abrupt events can be observed at lower $\dot{\varepsilon}_a$, as illustrated in Fig. 3(b). The magnification of the raw *F(t)*-curve in a shorter time interval, where the work hardening does not fully obstruct the details (Fig. 4), makes it clear that such abrupt events represent steps and drops resembling discontinuities observed during jerky flow of various materials [27]. This qualitative change in the shape of the deformation curves upon changing the strain rate testifies that the observed signals cannot be fully accounted for by either a random or instrumental noise but contain information on plasticity processes. This conjecture is confirmed by the results of the fast Fourier transform (FFT) for such signals, as illustrated in Figs. 3(c)-(d). The force fluctuations recorded at 10^{-3} s^{-1} render a broad-band power spectrum with multiple components covering two orders of magnitude of frequency, f (approximately from 0.01 Hz to 1 Hz). Such patterns evoke dynamical chaos, which is characterized by broad spectra with a large number of frequencies [29].

In contrast, the signal for 10^{-5} s^{-1} renders a spectrum fluctuating around a power-law dependence, $P(f) \sim f^{\gamma}$. Its slope, γ, takes on a value of about - 1.8, intermediate between the values related to the pink (also called 1/*f*) noise and Brown (random walk) noise corresponding to the $1/f^2$ spectrum. The 1/*f* noise, designating more generally any noise with $-2 < \gamma < 0$, characterizes various complex phenomena from different fields of science and was also found for the jerky flow [33,45]. It is noteworthy that $1/f^2$ spectrum may also appear for some kinds of complex behaviors, e.g., for the well-known phenomenon of the self-organized criticality often applied to explain the power-law statistics of deformation processes [33,44]. To avoid confusion, it should be mentioned that while the power-law behavior is associated with the scale invariance, the spectrum of Fig. 3(d) also displays multiple harmonics around the power-law trend, which reveals the presence of characteristic frequencies. Similar spectra were found for the strain rates of 10^{-4} s^{-1} and 10^{-6} s^{-1},

with γ varying between - 1.5 and - 2. Finally, all spectra tend to a flat dependence characteristic of the stochastic behavior (white noise) in the limit of high frequencies.

The results of the complexity analysis of the $F(t)$ signals are presented in Fig. 5 for all $\dot{\varepsilon}_a$. It was found that in general, the sample entropy increased with respect to the scale factor, which indicates complex behavior across multiple time scales. For $\dot{\varepsilon}_a = 10^{-3}$ s^{-1}, the sample-entropy curve displayed a maximum at a scale factor of 6. Similar behavior was earlier found for the serrated flow and ascribed to chaotic dynamics [73]. Although the detection of dynamical chaos goes beyond the scope of this paper, it should be noted that the conjecture of chaos agrees with the above-mentioned observation of the multiperiodic character of the analyzed signal. The dependences obtained at other $\dot{\varepsilon}_a$ showed monotonously-ascending trends. This trend is similar to that characterizing the Brown noise but the experimental dependences find themselves in the intermediate positions between those for Brown and pink noise [74]. For the pink noise, the entropy varies about the level of 2 for all values of the scale factors. The entropy of the force signals approaches this level at large scales, i.e., in the low-frequency limit. Thus, the overall results of the RCMSE analysis are qualitatively consistent with the FFT results [Figs. 3(c)-(d)].

Furthermore, it may be noticed that the dependences became steeper when $\dot{\varepsilon}_a$ was decreased from 10^{-4} s^{-1} to 10^{-6} s^{-1}. This variation agrees with the concomitant increase in the apparent contribution of abrupt events to the force signals [see Figs. 3(a)-(b)]. At the same time, Table 1 shows that the *CI* did not change monotonously. Based on the results, the overall complexity was the greatest for $\dot{\varepsilon}_a = 10^{-3}$ s^{-1} and passed a minimum at $\dot{\varepsilon}_a = 10^{-5}$ s^{-1}.

To ascertain that this result was not biased because of the presence of random noise, additional verifications were made with the aid of the *R*/*S* and statistical analyses, presented in Fig. 6. The *R*/*S* dependence obtained for the highest $\dot{\varepsilon}_a$ is bent everywhere, perhaps, asymptotically

approaching a straight line at the smallest time scale. The absence of a significant straight interval means that the signal does not manifest global scaling features. Nevertheless, the estimate of the Hurst exponent [66], H, as the steepness of the extrapolated slope at small scales may indicate a persistent, correlated behavior for short delays ($H > 0.5$). The dependences found for intermediate strain values show a good scaling in a large interval, with close H values corresponding to anti-persistent behavior ($H < 0.5$, see Table 1). However, when $\dot{\varepsilon}_a$ is further decreased, the scaling interval becomes relatively reduced again, and the respective H estimate is larger than 0.5.

Figure 6(b) displays the probability density of the fluctuation amplitude, ΔF, for the $F(t)$ signals. In contrast to the previously-considered characteristics, the amplitude distribution does not contain the information on the temporal correlations. Interestingly, it also shows nonmonotonous changes with $\dot{\varepsilon}_a$. For $\dot{\varepsilon}_a = 10^{-3}$ s^{-1}, the PDF is descending everywhere and shows a conspicuous interval of the power-law behavior as $D(\Delta F) \sim \Delta F^{-\beta}$. The behavior for 10^{-4} s^{-1} exhibits two distinct scales – a large asymmetrical peak with a maximum slightly above 0.1 N and a narrow peak about 0.8 N. The large peak persists at 10^{-5} s^{-1}, although the scale separation becomes less pronounced. More exactly, the right peak disappears, but the probability has an elevated value at 0.9 N. The emergence of a characteristic scale for the largest amplitudes can be attributed to the abrupt events occurring at low $\dot{\varepsilon}_a$ and may even be related to the tendency to the Brown noise for $\dot{\varepsilon}_a \leq 10^{-4}$ s^{-1}. It is all the more interesting that the PDF resumes the persistently-descending character at 10^{-6} s^{-1} and can be tentatively fitted with a power-law dependence in some range of amplitudes. This change is likely due to the occurrence of such events with amplitudes in intermediate ranges.

While the above analyses considered global features of the signals, the MF analysis has a more local character, as it searches for subsets corresponding to different scaling properties. Its

result thus depends on the repartition of the signal features along the time axis. Figures 7(a)-(b) display the results of such analysis for the force signals recorded at 10^{-3} s^{-1} and 10^{-6} s^{-1}. The left figure shows examples of scaling dependences of partition functions, $Z_f(\delta t)$ [see Eq. (11)], for several q values for 10^{-3} s^{-1}. The dependences do not exhibit an overall scaling, in agreement with the results of the R/S analysis. Nevertheless, two short scaling intervals can be detected. The left interval (dotted line) corresponds to the frequency range of about 1 - 5 Hz, fitting the part of the power spectrum characterized by a large number of frequencies [cf. Fig. 3(c)]. Despite its shortness, the calculation renders a smooth shape for the singularity spectrum [solid circles in Fig. 7(b)].

Moreover, it can be recognized that $f(\alpha)$ does not tend to zero on the left side, but corresponds to a finite positive value, $f(\alpha) \approx 0.4$. This feature is usually attributed to the presence of multiple oscillations in the signal [28], which is consistent with the above remark on the FFT spectrum. Furthermore, this tendency to scaling behavior for the fine-scale range agrees with the increasing complexity at small scales (cf. Fig. 5). The span of the second family of straight lines is quite narrow, which leads to a tendency to collapsing of the singularity spectrum (open circles) and bears evidence that nonfractal behavior is approached. The latter may correspond to close-to-periodic oscillations, giving rise to the large peak around 0.3 Hz in the power spectrum [cf. Fig. 3(c)].

In contrast to the highest $\dot{\varepsilon}_a$, the families of the partition functions were noisier, and smooth MF spectra were not detected at intermediate strain rates. Nevertheless, the partition functions globally showed similar trends as in Fig. 7(a). Relatively-good MF spectra were found again at 10^{-6} s^{-1}, as illustrated by the dependence marked by crosses in Fig. 7(b). Therewith, both

the increase in the span of α and the approach of $f(\alpha)$ to zero on the left side of the MF spectrum indicate more heterogeneous behavior than at 10^{-3} s^{-1}.

3.3 Local strain-rate signals

For each test, the analysis of the complexity of the local strain-rate signals was performed for several distant sites on the specimen surface, located within different grains. The found trends occurred to be qualitatively similar for different sites, thus indicating that the nature of the complexity may not depend on the initial grain orientation, at least, at the stage of stabilized evolution of the local strain heterogeneity (see Section 3.1). The further illustrations (Figs. 8 and 9) are presented for the sites situated in the middle of the specimens on the vertical symmetry axes. Surprisingly, in contrast to the force, $d\varepsilon_{loc}/dt$ signals display similar features at all strain rates. Moreover, their behavior is qualitatively different from various behaviors found for the force fluctuations. Figure 8(a) presents the local $d\varepsilon_{loc}/dt$ signal for $\dot{\varepsilon}_a = 10^{-5}$ s^{-1}. The corresponding power spectrum shows a power-law increase in a large frequency interval from 0.001 Hz to 0.3 Hz. Moreover, at higher frequencies (0.01 – 0.3 Hz), $P(f)$ exhibits variations about a linear trend on log-log coordinates. Signals with such a spectrum are usually associated with the blue noise [65,75]. More specifically, this term is applied to signals, whose power density increases proportionally to the frequency. In this narrow sense, the power spectrum shown in Fig. 8(b) finds itself between blue and violet (f^2) kinds of noise, as illustrated by the dashed line corresponding to a dependence of $P(f) \sim f^{1.5}$.

The relation of the local behavior of the plastic flow to blue noise was verified, using various analyses. Notably, blue noise indicates anti-persistence with the Hurst exponent, $H \approx 0$ [65]. Indeed, a close-to-zero H was found for $d\varepsilon_{loc}/dt$ signals at all strain rates. The results of the complexity analysis for the generated blue and white noise, and for two examples of the recorded

$d\varepsilon_{loc}/dt$ signals, are featured in Fig. 9(a). The latter examples approximately bound the domain of variation of the entropy dependences for the entirety of tests. It is seen that the dependences radically differed from those for the force signals. Namely, the sample entropy decreased with respect to the scale factor for all conditions. Such a trend suggests that the fluctuations do not contain complex structures across multiple scales [76]. Overall, the local response to the plastic flow behaves like a blue noise.

This finding was also confirmed by the comparison of the respective PDFs of the normalized amplitudes of fluctuations exhibited by the signals [Fig. 9(b)]. The representation in terms of the probability density for the normalized amplitude was used instead of conventional histograms to combine both dependences in one plot. Accordingly, both datasets can be described by similar curves corresponding to positively-skewed distributions, which display a Gaussian-like behavior on the right-hand side, without peculiarities at large scales. Finally, the MF analysis of the local signals also revealed that the trends found for the partition functions are similar for the blue noise and the experimental time series. However, the MF structure was not reliably detected for these signals.

3.4 Acoustic emission

Figure 10 illustrates the results of the AE measurements for the same sample, as presented in Fig. 1 of the main text, deformed at 10^{-3} s^{-1}. The graphs put into context the deformation curve, as presented in terms of the time-dependent force [Fig. 10(a)], the logarithmic amplitudes of the recorded AE hits [Fig. 10(b)], and their cumulated amplitudes [Fig. 10(c)]. The data of the figure testify that both the intensity and the activity of the AE are weak in comparison with conventional alloys, in particular, Al-based alloys, which are also prone to jerky flow caused by the Portevin-Le Chatelier (PLC) effect and show much stronger AE during both jerky and smooth flow [77].

Indeed, only a small number of AE events is observed within a range of relatively-small amplitudes, mostly below 50 dB, except for the event accompanying the fracture of the sample. The conclusion on the weak AE was valid for all samples. This conclusion is consistent with the low intensity of strain localization, as reflected in the virtual absence of significant bursts in the local strain-rate fluctuations [cf. Fig. 8(a)]. Moreover, when $\dot{\varepsilon}_a$ was decreased, the AE activity became progressively weaker. At first glance, the suppression of the AE contradicts the occurrence of larger force fluctuations at small strain rates [cf. Fig. 3(b)]. However, it can be noticed that even if these fluctuations look abrupt at the scale of the figure, their kinetics are slowed down in proportion to $\dot{\varepsilon}_a$, so that they may not correlate with the occurrence of audible sounds.

Despite the relative "silence" of the plastic flow in the studied alloy, the observed AE undoubtedly reflects plastic-deformation processes. This trend certainty follows, e.g., from the observation of an approximate similitude between the evolution of the cumulated amplitude [Fig. 10(c)] and the deformation curve [Fig. 10(a)]. It is also noteworthy that the AE is stronger at the beginning of deformation and decreases during the test presented in this figure. Such behavior is typical of many materials and is usually explained by the work hardening leading to a reduction in the dislocation free-flight distance. In the case of the studied alloy, it may also be suggested that there exists a relationship between the decrease in the AE and the weakening of the strain localization after some straining [cf. Fig. 1(b)]. The possible role of the degree of strain localization was also indicated by an observation, for some samples, of a step on the cumulated AE-amplitude curve in the region of the inflection of the deformation curve. Such a step, although rather small for the discussed sample, is discernible around 150 s in Fig. 10(c).

At the same time, these observations were not unique for all samples. In some cases, the AE appeared to be intensified during deformation. Such a trend worsened the similitude between

the cumulated amplitude and the deformation curve. In view of the weakness of the AE, the variations observed may indicate a significant role of the haphazard factor related to the heterogeneity of the initial microstructure, e.g., to the repartition of the so-called "weak spots" [26] where the slip will be predominant.

Importantly, it was found that the series of AE hits obey power-law distributions in all conditions. Figure 11 illustrates the log-log plot of the PDF, $D(W) \sim W^{-\beta}$, for $\dot{\varepsilon}_a = 10^{-3}$ s^{-1}, where W characterizes the normalized AE energy, $W = A^2/\langle A^2 \rangle$, A is the amplitude of an individual hit, and $\langle A^2 \rangle$ is the average value over the series of hits [45]. The values of β found for various tests varied approximately between 1.5 and 2.1.

The power-law statistics of the AE have been reported for numerous materials, for both smooth and jerky flows [44,45,47]. As said in the Introduction section, these findings have led to a conclusion on an inherent avalanche nature of the dislocation dynamics at the scales relevant to the AE. Thus, the present data allow for a conjecture that at this scale, the deformation behavior of the studied HEA alloy belongs to the same class of collective dynamics as in the case of conventional materials.

4. Discussion

It is known that the plastic deformation of pure materials and solute alloys manifests a collective nature at different scales, from the fine range accessible by virtue of the AE technique [43–45,57] to a coarser range unveiled by various methods of local extensometry [43,50,52–54], and even at the macroscopic level, as in the case of jerky flows (e.g., [28,33,78]). Jerky flow has also been observed and investigated for various HEAs [3]. However, as their crystal lattice is extremely distorted, which makes more difficult the motion of dislocations, it cannot be stated *a priori* whether the collective effects emerge on finer scales in the dislocation dynamics of HEAs.

The objective of the present work is to detect such effects in an HEA in the absence of the macroscopic jerky flow, compare their manifestations on distinct scales, and apply the obtained dynamical characteristics to shed additional light on the physics of plasticity in these novel materials. Moreover, as the local strain fields have been little explored for conventional materials from the viewpoint of self-organization, the present investigations have a more general meaning for understanding the plastic flow of solids.

The analysis of the AE revealed a feature well known for various materials, namely, power-law distributions of the hits amplitude (Fig. 11). This result is usually interpreted in terms of the avalanche-like collective dynamics of dislocations [33,44]. It can thus be suggested that the correlations of dislocations in HEAs lead to the same "elementary" collective processes – avalanches – as in conventional materials.

According to the literature, only a part of dislocations participate in strongly-correlated avalanche processes giving rise to discrete AE recorded as individual hits, whereas the other part perform less correlated motions producing a continuous acoustic noise [44]. The low amount of AE hits recorded in the present tests (cf. Fig. 10) suggests a relatively-weak correlation of dislocations in the investigated alloy. Since the repartition of the dislocations performing correlated or uncorrelated motions depends on the symmetry of the crystal lattice and microstructure, the weak AE activity in the HEA with an *fcc* lattice is consistent with the observations of a predominantly-continuous AE in *fcc* metals, such as Cu or Al [44]. On the other hand, it was reported that AlMg alloys, prone to jerky flow caused by the PLC effect, exhibit much AE activity even during macroscopically-smooth deformation [47, 56, 74]. It is thus reasonable to consider alternative causes, as well. Two possible factors should be mentioned in this context: (i) The limitation of the dislocation mobility in HEAs because of the strong distortion of their crystal

lattice, similar to a strong reduction in the AE of AlMg alloys upon grain refinement [45]; and (ii) A strong sound attenuation, also caused by the specific microstructures of HEAs [79].

In contrast to these results, one of the most unexpected findings came from the analysis of the local strain-rate signals that displayed patterns very close to the blue noise at all strain rates. A blue noise emerges much rarer in the natural phenomena than 1/*f* noise. In particular, it has not been reported for the plastic flow, perhaps, because only few papers considered the evolution of the local strain rate in conventional materials, e.g., in Cu single crystals [43,50] or AlMg polycrystals [53]. According to these investigations, the power-law statistics describe both the AE and the local strain-rate fluctuations. The behavior found in the present work is qualitatively different. It should be mentioned, however, that the one-dimensional local extensometry method used in [43,50,53] had at least one order of magnitude higher temporal and spatial resolution than the 2D DIC applied here. This comparison rises a challenging question and will require to extend studies with different extensometry methods to materials with distinct crystal symmetries and defect microstructures.

Some hypotheses may be proposed as to the specific behavior of the local strain rate in the HEA alloy. The blue noise means a fully-anti-persistent, negatively-correlated behavior. To interpret the negative correlation, it should be underlined that in contrast to the AE that gathers the global information from the entire specimen, $d\varepsilon_{loc}/dt$ is related to a small element on the specimen surface (see Section 2.3.1). Taking into account the shear character of the plastic flow (see Fig. 2), the local response must reflect deformation processes in a narrow cross-section. Its anti-persistence may be explained by the local strain hardening, which would force the transfer of the plastic deformation to other sites within the grain or to neighboring grains. The latter process is clearly seen on both optical images of a specimen cross-section and on the corresponding geometrically

necessary dislocation (GND) maps in Fig. A1. At the same time, Fig. 1(b) testifies that the plastic flow is intially localized in several zones. That is, while the plastic flow is anti-persistent with regard to temporal correlations at a given site, it is persistent on a coarser spatial range. This persistence is conform to the relatively-low initial work-hardening rate [Fig. 1(a)]. The work hardening becomes faster after some deformation, in agreement with the observation of a more uniform plastic flow. Nevertheless, the strain delocalization is not complete, and traces of such active zones persist through the entire map of Fig. 1(b). The overall pattern might be attributed to the large grain size in the studied material, so that the low work hardening and stronger strain localization would correspond to the plastic flow in one slip system in individual grains (analog of the easy glide in single crystals), while further changes would be related to the activation of more slip systems. Indeed, Figs. A1 (a) and (b) show strain localization in some grains and the predominace of a single slip [see Fig. A1 (b)] at a strain value close to the inflection point on the deformation curve, whereas Figs. A1 (c) and (d) reveal multiple slip [see Fig. A1 (d)] and the spread of the plastic activity to many grains after deformation to a large strain. Therewith, the comparison of Figs. A1 (b) and (d) shows similar values of GND densities varying between 10^{13} and 5×10^{14} m^{-2} for both deformation levels (the GND density was negligible in the initial material as no disorientation was detected). However, these data do not suffice for a definite conclusion on the mechanism of the observed deformation behavior. For example, a similar three-stage shape of deformation curves was also observed in Ref. [55] for a polycrystalline HEA from the same family with a grain size of about 40 μm. Attention may also be attracted to the observaton of persistent strain-localization zones in noncrystalline BMGs, which are characterized by strain softening, e.g., because of the free-volume generation or liquid-like effects [3,37]. Thus, it may be asked whether the specific crystal structure of HEAs may lead to effects of a locally decreased work-hardening

capacity. To answer this question, further experiments will be needed, in particular, *in situ* investigations of the microstructure evolution, as well as DIC experiments on HEAs with finer polycrystalline structures.

Another challenging question concerns the observation of a qualitatively similar complexity of the local signals gathered from sites situated in different grains. It may be supposed that such virtual independence of the complexity on the grain orientation is due to the condition that the analysis has to be performed for stabilized behavior which is attained in the strain range corresponding to the multiple dislocation glide. However, it cannot be excluded *a priori* that the blue-noise-like nature of the complexity is due to the interactions between mobile dislocations in the same slip system. Meanwhile, the exact crystallography of the dislocation glide as well the interactions with forest dislocations may play less significant roles, perhaps, giving rise to quantitative variations of the studied dependences. Extending the analyses to characterize the initial transitory behaviors and a meticulous quantitative study of their dependences on the grain orientations will be needed to shed further light on this question.

Furthermore, in contrast to AE and DIC each displaying a unique (but distinct from each other) type of behavior at all strain rates, the processing of the force signals revealed various apparent dynamics depending on $\dot{\varepsilon}_a$. The major finding is that the move to a coarser scale and from a local to a global observable quantity changed the apparent behavior from blue to reddened noises, the latter testifying to more persistent behavior. A possible explanation of the emerging correlations may be suggested in the spirit of the concept proposed to explain the transitions between distinct types of jerky flow (e.g., [33,56,74]), which considered the effect of $\dot{\varepsilon}_a$ on the efficiency of relaxation of internal stresses recurrently generated during the heterogeneous plastic flow. Accordingly, as quantified by the *CI*, the most complex behavior was found for the highest

$\dot{\varepsilon}_a$, i.e., when the internal stresses generation dominates over their relaxation, so that the material finds itself in a highly-heterogeneous state. The FFT and RCMSE analyses showed a wide power spectrum [Fig. 3(c)] and a nonmonotonous entropy variation with the scale factor (Fig. 5). These features are often associated with chaotic behavior. The hypothesis of chaos was also corroborated by the multifractality detected for the fine time scale, which confirmed the presence of multiple spectral components in the signal (Fig. 7). However, the *R*/*S* method did not reveal global scaling behavior [Fig. 6(a)], in agreement with a nonunique scaling uncovered by the MF analysis. Besides, whereas chaos in the jerky flow was usually associated with distributions of stress serrations exhibiting several peaks [33], Fig. 6(b) demonstrates a monotonously-descending distribution with a clear interval of the power-law dependence and a slope typical of avalanche processes [43,44]. It may thus be supposed that the high strain-rate behavior does not correspond to a unique dynamical mode. Further investigations will be needed to caracterize such a transitory dynamics.

When $\dot{\varepsilon}_a$ is decreased, the relaxation of the internal stresses becomes more efficient and leads to the uniformization of the stress field. Accordingly, the elements of the material finding themselves in a similar state tend to deform collectively. This synchronization would lead to an emergency of a characteristic scale, which might explain the peaked distributions for 10^{-4} s^{-1} and 10^{-5} s^{-1} [Fig. 6(b)]. Moreover, the histograms show an increase in the probability of large events. Such a phenomenon was also reported for jerky flows at low $\dot{\varepsilon}_a$ [53,77,78]. It was conjectured that when a dislocation avalanche is powerful enough, it can trigger the sequence of avalanches and result in a “catastrophic” event with a drastically-enhanced amplitude. Interestingly, despite this scale separation in the distributions of the events amplitudes, the analyses assessing temporal correlations uncovered the presence of a global scaling in the force signals for the same strain rates

(see Figs. 3 and 5). On the whole, the FFT, *R*/*S*, and RCMSE methods attest these signals as the intermediate between pink and Brown noise.

Unexpectedly, these changes do not show all the same trends when $\dot{\varepsilon}_a$ is further decreased. Notably, the scale separation is suppressed in the amplitude distributions, which become monotonously decreasing, the *R*/*S* analysis indicates a positive correlation ($H > 0.5$) for a relatively-short τ, and the RCMSE analysis testifies to an increased complexity. It may be supposed that the further uniformization of the strain-stress field makes more probable the triggering effect in different regions of the material and begets events of various sizes. This conjecture is conformed to the new emergence of the multifractality at 10^{-6} s^{-1}. Therewith, the MF spectrum becomes larger than at the high strain rate (cf. [80,81] for the serrated flow).

Since the background concept of the relaxation of the internal stress heterogeneity has first been suggested as one of two factors governing the dynamics of the jerky flow, it would be enlightening to deepen the started comparison. The macroscopic-plastic instability displays similar trends in HEAs and conventional materials [3] and is believed to be related to the same mechanism of pinning/unpinning of dislocations from clouds of solute atoms (e.g., [29]). This mechanism converts the positive SRS dependence slope into a nonlinear *N*-shaped function with an interval of negative slope and, therefore, implies a threshold dynamics. This additional factor may be of great importance. For example, the need to overcome a threshold may promote the phenomenon of scale separation in the statistical distributions at low $\dot{\varepsilon}_a$ because only powerful enough avalanches will be able to follow the triggering process, so that the events with medium amplitudes will not occur. Indeed, the available literature reports that large stress serrations are preponderant at very low strain rates, in contrast to the present results, but in agreement with the prediction of relaxation oscillations determined by the *N*-shaped function [29,33,77]. Moreover, various alloys

studied so far showed qualitatively similar sequences of transitions from such synchronized oscillations to chaotic dynamics at medium $\dot{\varepsilon}_a$-values, and to power-law statistics at the highest $\dot{\varepsilon}_a$. In contrast, the changes observed in the present paper are more intricate and seem to allow for various combinations of distinct dynamical regimes.

5. Conclusions

In summary, a multiscale approach to the investigation of the complexity of the plastic flow of a HEA allowed to obtain new information on the little studied mesoscopic scale of plasticity, which is governed by collective dislocation processes. One of the main perceptions is that the plastic flow manifests self-organization of dislocations even in the absence of the macroscopic collective effects giving rise to a jerky flow. Meaningful inferences follow from a comprehensive comparison of different aspects of these fine-scale behaviors with the akin data for the macroscopic plastic instability. Hence, the visualization of the local strain-rate field revealed a similitude between the shear-like geometry of the strain localization during a smooth and jerky flow. At the same time, the analyses of the force fluctuations about the macroscopically-smooth trend uncover complex behaviors, which display both similar and distinct features, compared to those for the jerky flow, and are likely to have a transitory nature due to the combination of various kinds of the nonlinear dynamics. Moreover, the same analyses applied to the signals pertaining to distinct physical scales in the mesoscopic range – the acoustic emission, the local strain rate, and the force responses – prove that the consequences of the dislocations self-organization show up differently in various scale ranges. In particular, the power-law distribution of the acoustic energy reflects an avalanche-like dynamics of dislocations and unifies the fine-scale behavior of the HEA with similar behaviors of all materials studied so far. In contrast, the behavior of the local strain-rate field occurs to be close to the blue noise. Such dynamics is rare in natural systems and has

never been reported for plastic deformation. Surprisingly, a transition from the blue to reddened kinds of noise is observed upon moving from this local characteristic to the analysis of the force fluctuations. This remarkable variety of behaviors underlines that the knowledge of the nonlinear dynamics related to such fine scales in both HEA and conventional materials is a challenge for the further progress in the understanding and modeling of mechanical behavior of crystals.

Acknowledgements. M.L. and T.L gratefully acknowledge the support from the French State through the program "Investment in the future" operated by the National Research Agency, in the framework of the LabEx DAMAS [ANR-11-LABX-0008-01]. P.K.L. greatly thanks the support from (1) the National Science Foundation (DMR-1611180 and 1809640) and (2) the Army Research Office (W911NF-13-1-0438 and W911NF-19-2-0049).

Author contributions. M.L., J.B., and P.K.L. conceived and designed the experiments, R.F. fabricated samples, R. F., T.L., and M.L. performed the mechanical, DIC, and AE tests, B.B. and H.J. performed the microstructure analysis, J.B., H.J., T.L., and M.L. conducted the analyses of the experimental data, J.B., R.F., P.K.L., and M.L. helped write the manuscript and carried out text editing. All the authors discussed the results and commented on the manuscript.

Competing interests. The authors declare no competing financial interests.

Data Availability Statement: The raw/processed data required to reproduce these findings cannot be shared at this time due to legal or ethical reasons.

Appendix

Optical microscopy, Back-Scattered Electron (BSE) imagery, and Electron Back-Scattered Diffraction (EBSD) were used to characterize the microstructure in the initial and deformed samples and the plastic activity at different strain levels. Figures A1(a) and (c) present examples

of optical images obtained after deformation to strains of 15.9% and 43.3%. Their counterparts in the images (b) and (d) show the repartition of the density of geometrically necessary dislocations (GND) for the regions sketched in the BSE images, as calculated from the EBSD data.

To accomplish this task, the electron-microscopy data were acquired, using a FEG-SEM JEOL F100 equipped with an Oxford Symmetry camera. The sample to detector distance was 15 mm, and the accelerating voltage was 15 kV. The step size was set to 0.3 μm for the deformed samples in order to calculate the GND densities with a sufficient spatial resolution. A larger step size of 7 μm was used for the initial material, which had grains with a homogeneous orientation (not presented here). The EBSD patterns were then indexed by the commercial Aztec software producing crystallographic-orientation maps. Using the orientation maps, GND densities can be depicted from the Nye tensor, $\boldsymbol{\alpha} \cong tr(\boldsymbol{\kappa}).\boldsymbol{I} - \boldsymbol{\kappa}^T$, where $\boldsymbol{\kappa}$ is the elastic curvature obtained from the disorientations [82,83]. The Nye tensor was calculated by the ATEX software developed in the Lorraine university [84].

The images A1(b) and (d) display the entrywise norm of the so-calculated Nye tensor normalized by the Burgers vector length, $\|\boldsymbol{\alpha}\| \cong \frac{\mathbf{1}}{\boldsymbol{b}}\sqrt{\alpha_{ij}\alpha_{ij}}$. It may be noted as a matter of example that after deformation, large disorientations up to 30° from one to the other side of a grain can be found in the inverse pole figures (not shown), thus revealing a strong plastic activity. It can be recognized in the presented GND maps that the GND densities vary in the same range of 10^{13} to 5 × 10^{14} m^{-2} in the samples deformed to different levels. At the same time, these figures testify to a strongly localized GND distribution at a low strain, while all visible grains exhibit plastic activity after strong deformation. As the large grain size makes it impossible to display entire grains with a high spatial resolution in the GND maps, the last claim is corroborated by the respective BSE images presented on a coarser scale.

6. References

[1] J.-W. Yeh, S.-J. Lin, T.-S. Chin, J.-Y. Gan, S.-K. Chen, T.-T. Shun, C.-H. Tsau, S.-Y. Chou, Formation of simple crystal structures in Cu-Co-Ni-Cr-Al-Fe-Ti-V alloys with multiprincipal metallic elements, Metallurgical and Materials Transactions A. 35 (2004) 2533–2536.

[2] B. Cantor, I.T.H. Chang, P. Knight, A.J.B. Vincent, Microstructural development in equiatomic multicomponent alloys, Materials Science and Engineering: A. 375–377 (2004) 213–218.

[3] J. Brechtl, S. Chen, C. Lee, Y. Shi, R. Feng, X. Xie, D. Hamblin, A.M. Coleman, B. Straka, H. Shortt, R.J. Spurling, P.K. Liaw, A review of the serrated-flow phenomenon and its role in the deformation behavior of high-entropy alloys, Metals. 10 (2020).

[4] D.B. Miracle, High entropy alloys as a bold step forward in alloy development, Nature Communications. 10 (2019) 1805.

[5] C. Lee, G. Kim, Y. Chou, B. L. Musicó, M. C. Gao, K. An, G. Song, Y.-C. Chou, V. Keppens, W. Chen, P. K. Liaw, Temperature dependence of elastic and plastic deformation behavior of a refractory high-entropy alloy, Science Advances. 6 (2020) eaaz4748.

[6] M. Todai, T. Nagase, T. Hori, A. Matsugaki, A. Sekita, T. Nakano, Novel TiNbTaZrMo high-entropy alloys for metallic biomaterials, Scripta Materialia. 129 (2017) 65–68.

[7] W. Yang, Y. Liu, S. Pang, P.K. Liaw, T. Zhang, Bio-corrosion behavior and in vitro biocompatibility of equimolar TiZrHfNbTa high-entropy alloy, Intermetallics. 124 (2020) 106845.

[8] Y. Shi, B. Yang, P.K. Liaw, Corrosion-resistant high-entropy alloys: A review, Metals. 7 (2017).

[9] T. Egami, W. Guo, P.D. Rack, T. Nagase, Irradiation Resistance of Multicomponent Alloys, Metallurgical and Materials Transactions A. 45 (2014) 180–183.

[10] Y. Zhang, G.M. Stocks, K. Jin, C. Lu, H. Bei, B.C. Sales, L. Wang, L.K. Béland, R.E. Stoller, G.D. Samolyuk, M. Caro, A. Caro, W.J. Weber, Influence of chemical disorder on energy dissipation and defect evolution in concentrated solid solution alloys, Nature Communications. 6 (2015) 8736.

[11] O. El-Atwani, A. Alvarado, K. Unal, S. Fensin, J.A. Hinks, G. Greaves, J.K.S. Baldwin, S.A. Maloy, E. Martinez, Helium implantation damage resistance in nanocrystalline W-Ta-V-Cr high entropy alloys, Materials Today Energy. 19 (2021) 100599.

[12] M.-H. Chuang, M.-H. Tsai, W.-R. Wang, S.-J. Lin, J.-W. Yeh, Microstructure and wear behavior of $Al_xCo1.5CrFeNi1.5Ti_y$ high-entropy alloys, Acta Materialia. 59 (2011) 6308–6317.

[13] M.-H. Chuang, M.-H. Tsai, C.-W. Tsai, N.-H. Yang, S.-Y. Chang, J.-W. Yeh, S.-K. Chen, S.-J. Lin, Intrinsic surface hardening and precipitation kinetics of $Al_{0.3}CrFe_{1.5}MnNi_{0.5}$ multi-component alloy, Journal of Alloys and Compounds. 551 (2013) 12–18.

[14] K.V.S. Thurston, B. Gludovatz, A. Hohenwarter, G. Laplanche, E.P. George, R.O. Ritchie, Effect of temperature on the fatigue-crack growth behavior of the high-entropy alloy CrMnFeCoNi, Intermetallics. 88 (2017) 65–72.

[15] P. Chen, C. Lee, S.-Y. Wang, M. Seifi, J.J. Lewandowski, K.A. Dahmen, H. Jia, X. Xie, B. Chen, J.-W. Yeh, C.-W. Tsai, T. Yuan, P.K. Liaw, Fatigue behavior of high-entropy alloys: A review, Science China Technological Sciences. 61 (2018) 168–178.

[16] R. Feng, Y. Rao, C. Liu, X. Xie, D. Yu, Y. Chen, M. Ghazisaeidi, T. Ungar, H. Wang, K. An, Peter.K. Liaw, Enhancing fatigue life by ductile-transformable multicomponent B2 precipitates in a high-entropy alloy, Nature Communications. 12 (2021) 3588.
[17] X. Gao, Y. Lu, B. Zhang, N. Liang, G. Wu, G. Sha, J. Liu, Y. Zhao, Microstructural origins of high strength and high ductility in an $AlCoCrFeNi_{2.1}$ eutectic high-entropy alloy, Acta Materialia. 141 (2017) 59–66.
[18] B. Cai, B. Liu, S. Kabra, Y. Wang, K. Yan, P.D. Lee, Y. Liu, Deformation mechanisms of Mo alloyed FeCoCrNi high entropy alloy: In situ neutron diffraction, Acta Materialia. 127 (2017) 471–480.
[19] C. Lee, F. Maresca, R. Feng, Y. Chou, T. Ungar, M. Widom, K. An, J.D. Poplawsky, Y.-C. Chou, P.K. Liaw, W.A. Curtin, Strength can be controlled by edge dislocations in refractory high-entropy alloys, Nature Communications. 12 (2021) 5474.
[20] Q. Pan, L. Zhang, R. Feng, Q. Lu, K. An, A. C. Chuang, J. D. Poplawsky, P. K. Liaw, L. Lu, Gradient cell–structured high-entropy alloy with exceptional strength and ductility, Science. 374 (2021) 984–989.
[21] D. Li, C. Li, T. Feng, Y. Zhang, G. Sha, J.J. Lewandowski, P.K. Liaw, Y. Zhang, High-entropy $Al_{0.3}CoCrFeNi$ alloy fibers with high tensile strength and ductility at ambient and cryogenic temperatures, Acta Materialia. 123 (2017) 285–294.
[22] P. Shi, R. Li, Y. Li, Y. Wen, Y. Zhong, W. Ren, Z. Shen, T. Zheng, J. Peng, X. Liang, P. Hu , N. Min, Y. Zhang, Y. Ren, P. K. Liaw, D. Raabe, Y.-D. Wang, Hierarchical crack buffering triples ductility in eutectic herringbone high-entropy alloys, Science. 373 (2021) 912–918.
[23] Y. Bu, Y. Wu, Z. Lei, X. Yuan, H. Wu, X. Feng, J. Liu, J. Ding, Y. Lu, H. Wang, Z. Lu, W. Yang, Local chemical fluctuation mediated ductility in body-centered-cubic high-entropy alloys, Materials Today. 46 (2021) 28–34.
[24] Z. Lyu, X. Fan, C. Lee, S.-Y. Wang, R. Feng, P.K. Liaw, Fundamental understanding of mechanical behavior of high-entropy alloys at low temperatures: A review, Journal of Materials Research. 33 (2018) 2998–3010.
[25] B. Gludovatz, A. Hohenwarter, D. Catoor, E.H. Chang, E.P. George, R.O. Ritchie, A fracture-resistant high-entropy alloy for cryogenic applications, Science. 345 (2014) 1153–1158.
[26] Y. Zhang, J.P. Liu, S.Y. Chen, X. Xie, P.K. Liaw, K.A. Dahmen, J.W. Qiao, Y.L. Wang, Serration and noise behaviors in materials, Progress in Materials Science. 90 (2017) 358–460.
[27] M.A. Lebyodkin, T.A. Lebedkina, J. Brechtl, P.K. Liaw, Serrated Flow in Alloy Systems, in: J. Brechtl, P.K. Liaw (Eds.), High-Entropy Materials: Theory, Experiments, and Applications, Springer International Publishing, Cham, 2021: pp. 523–644.
[28] M.A. Lebyodkin, T.A. Lebedkina, A. Jacques, Multifractal Analysis of Unstable Plastic Flow, Nova Science, 2009.
[29] L.P. Kubin, C. Fressengeas, G. Ananthakrishna, Chapter 57 Collective behaviour of dislocations in plasticity, in: F.R.N. Nabarro, M.S. Duesbery (Eds.), Dislocations in Solids, Elsevier, 2002: pp. 101–192.
[30] V.V. Pustovalov, Serrated deformation of metals and alloys at low temperatures (Review), Low Temperature Physics. 34 (2008) 683–723.
[31] F. Yang, H. Luo, E. Pu, S. Zhang, H. Dong, On the characteristics of Portevin–Le Chatelier bands in cold-rolled 7Mn steel showing transformation-induced plasticity, International Journal of Plasticity. 103 (2018) 188–202.

[32] J. Brechtl, B. Chen, X. Xie, Y. Ren, J.D. Venable, P.K. Liaw, S.J. Zinkle, Entropy modeling on serrated flows in carburized steels, Materials Science and Engineering: A. 753 (2019) 135–145.
[33] M.S. Bharathi, M. Lebyodkin, G. Ananthakrishna, C. Fressengeas, L.P. Kubin, The hidden order behind jerky flow, Acta Materialia. 50 (2002) 2813–2824.
[34] G. Ananthakrishna, C. Fressengeas, M. Grosbras, J. Vergnol, C. Engelke, J. Plessing, H. Neuhäuser, E. Bouchaud, J. Planès, L.P. Kubin, On the existence of chaos in jerky flow, Scripta Metallurgica et Materialia. 32 (1995) 1731–1737.
[35] A.F. Rowcliffe, S.J. Zinkle, D.T. Hoelzer, Effect of strain rate on the tensile properties of unirradiated and irradiated V–4Cr–4Ti, Journal of Nuclear Materials. 283–287 (2000) 508–512.
[36] X. Xie, Y.-C. Lo, Y. Tong, J. Qiao, G. Wang, S. Ogata, H. Qi, K.A. Dahmen, Y. Gao, P.K. Liaw, Origin of serrated flow in bulk metallic glasses, Journal of the Mechanics and Physics of Solids. 124 (2019) 634–642.
[37] J. Brechtl, X. Xie, Z. Wang, J. Qiao, P.K. Liaw, Complexity analysis of serrated flows in a bulk metallic glass under constrained and unconstrained conditions, Materials Science and Engineering: A. 771 (2020) 138585.
[38] J. Moon, E. Tabachnikova, S. Shumilin, T. Hryhorova, Y. Estrin, J. Brechtl, P.K. Liaw, W. Wang, K.A. Dahmen, H.S. Kim, Unraveling the discontinuous plastic flow of a Co-Cr-Fe-Ni-Mo multiprincipal-element alloy at deep cryogenic temperatures, Phys. Rev. Materials. 5 (2021) 083601.
[39] J. Antonaglia, X. Xie, Z. Tang, C.-W. Tsai, J.W. Qiao, Y. Zhang, M.O. Laktionova, E.D. Tabachnikova, J.W. Yeh, O.N. Senkov, M.C. Gao, J.T. Uhl, P.K. Liaw, K.A. Dahmen, Temperature effects on deformation and serration behavior of high-entropy alloys (HEAs), JOM. 66 (2014) 2002–2008.
[40] H. Zhang, K.W. Siu, W. Liao, Q. Wang, Y. Yang, Y. Lu, In situ mechanical characterization of CoCrCuFeNi high-entropy alloy micro/nano-pillars for their size-dependent mechanical behavior, Materials Research Express. 3 (2016) 094002.
[41] J. Brechtl, S.Y. Chen, X. Xie, Y. Ren, J.W. Qiao, P.K. Liaw, S.J. Zinkle, Towards a greater understanding of serrated flows in an Al-containing high-entropy-based alloy, International Journal of Plasticity. 115 (2019) 71–92.
[42] J. Moon, E. Tabachnikova, S. Shumilin, T. Hryhorova, Y. Estrin, J. Brechtl, P.K. Liaw, W. Wang, K.A. Dahmen, A. Zargaran, J.W. Bae, H.-S. Do, B.-J. Lee, H.S. Kim, Deformation behavior of a Co-Cr-Fe-Ni-Mo medium-entropy alloy at extremely low temperatures, Materials Today. (2021).
[43] J. Weiss, T. Richeton, F. Louchet, F. Chmelik, P. Dobron, D. Entemeyer, M. Lebyodkin, T. Lebedkina, C. Fressengeas, R.J. McDonald, Evidence for universal intermittent crystal plasticity from acoustic emission and high-resolution extensometry experiments, Phys. Rev. B. 76 (2007) 224110.
[44] J. Weiss, W.B. Rhouma, T. Richeton, S. Dechanel, F. Louchet, L. Truskinovsky, From mild to wild fluctuations in crystal plasticity, Phys. Rev. Lett. 114 (2015) 105504.
[45] T.A. Lebedkina, D.A. Zhemchuzhnikova, M.A. Lebyodkin, Correlation versus randomization of jerky flow in an AlMgScZr alloy using acoustic emission, Physical Review E. 97 (2018) 013001.

[46] A.A. Shibkov, M.A. Lebyodkin, T.A. Lebedkina, M.F. Gasanov, A.E. Zolotov, A.A. Denisov, Millisecond dynamics of deformation bands during discontinuous creep in an AlMg polycrystal, Phys. Rev. E. 102 (2020) 043003.
[47] I.V. Shashkov, M.A. Lebyodkin, T.A. Lebedkina, Multiscale study of acoustic emission during smooth and jerky flow in an AlMg alloy, Acta Materialia. 60 (2012) 6842–6850.
[48] D. M. Dimiduk, C. Woodward, R. LeSar, M. D. Uchic, Scale-free intermittent flow in crystal plasticity, Science. 312 (2006) 1188–1190.
[49] F. F. Csikor, C. Motz, D. Weygand, M. Zaiser, S. Zapperi, Dislocation avalanches, strain bursts, and the problem of plastic forming at the micrometer scale, Science. 318 (2007) 251–254.
[50] C. Fressengeas, A.J. Beaudoin, D. Entemeyer, T. Lebedkina, M. Lebyodkin, V. Taupin, Dislocation transport and intermittency in the plasticity of crystalline solids, Phys. Rev. B. 79 (2009) 014108.
[51] R.J. McDonald, C. Efstathiou, P. Kurath, The Wavelike Plastic Deformation of Single Crystal Copper, Journal of Engineering Materials and Technology. 131 (2009).
[52] R.N. Mudrock, M.A. Lebyodkin, P. Kurath, A.J. Beaudoin, T.A. Lebedkina, Strain-rate fluctuations during macroscopically uniform deformation of a solution-strengthened alloy, Scripta Materialia. 65 (2011) 1093–1096.
[53] M. Lebyodkin, Y. Bougherira, T. Lebedkina, D. Entemeyer, Scaling in the Local Strain-Rate Field during Jerky Flow in an Al-3%Mg Alloy, Metals. 10 (2020).
[54] D. Yuzbekova, A. Mogucheva, D. Zhemchuzhnikova, T. Lebedkina, M. Lebyodkin, R. Kaibyshev, Effect of microstructure on continuous propagation of the Portevin–Le Chatelier deformation bands, International Journal of Plasticity. 96 (2017) 210–226.
[55] J.C. Rao, H.Y. Diao, V. Ocelík, D. Vainchtein, C. Zhang, C. Kuo, Z. Tang, W. Guo, J.D. Poplawsky, Y. Zhou, P.K. Liaw, J.Th.M. De Hosson, Secondary phases in $Al_xCoCrFeNi$ high-entropy alloys: An in-situ TEM heating study and thermodynamic appraisal, Acta Materialia. 131 (2017) 206–220.
[56] C. Solutions, VIC-2D [Computer software], Reference Manual. Columbia, SC: Correlated Solutions. (2009).
[57] M.A. Lebyodkin, N.P. Kobelev, Y. Bougherira, D. Entemeyer, C. Fressengeas, T.A. Lebedkina, I.V. Shashkov, On the similarity of plastic flow processes during smooth and jerky flow in dilute alloys, Acta Materialia. 60 (2012) 844–850.
[58] L. Adam, E. Bonhomme, C. Chirol, A. Proust, Benefits of acoustic emission for the testing of aerospace composite assemblies, 30th European Conference on Acoustic Emission Testing & 7th International Conference on Acoustic Emission Universityof Granada, 12-15 September 2012, www.ndt.net/EWGAE-ICAE2012/.
[59] E. Pomponi, A. Vinogradov, A. Danyuk, Wavelet based approach to signal activity detection and phase picking: Application to acoustic emission, Signal Processing. 115 (2015) 110–119.
[60] E. Agletdinov, D. Drozdenko, P. Harcuba, P. Dobroň, D. Merson, A. Vinogradov, On the long-term correlations in the twinning and dislocation slip dynamics, Materials Science and Engineering: A. 777 (2020) 139091.
[61] S.-D. Wu, C.-W. Wu, S.-G. Lin, K.-Y. Lee, C.-K. Peng, Analysis of complex time series using refined composite multiscale entropy, Physics Letters A. 378 (2014) 1369–1374.
[62] A.C. Iliopoulos, N.S. Nikolaidis, E.C. Aifantis, Analysis of serrations and shear bands fractality in UFGs, Journal of the Mechanical Behavior of Materials. 24 (2015) 1–9.

[63] M.D. Costa, A.L. Goldberger, Generalized multiscale entropy analysis: Application to quantifying the complex volatility of human heartbeat time series, Entropy. 17 (2015).
[64] M. Costa, A.L. Goldberger, C.-K. Peng, Multiscale entropy analysis of biological signals, Phys. Rev. E. 71 (2005) 021906.
[65] A. Omidvarnia, A. Zalesky, S. Mansour L, D. Van De Ville, G.D. Jackson, M. Pedersen, Temporal complexity of fMRI is reproducible and correlates with higher order cognition, NeuroImage. 230 (2021) 117760.
[66] J. Feder, Fractals, Springer US, 2013.
[67] M.A. Lebyodkin, T.A. Lebedkina, Multifractal analysis of evolving noise associated with unstable plastic flow, Phys. Rev. E. 73 (2006) 036114.
[68] T.C. Halsey, M.H. Jensen, L.P. Kadanoff, I. Procaccia, B.I. Shraiman, Fractal measures and their singularities: The characterization of strange sets, Phys. Rev. A. 33 (1986) 1141–1151.
[69] A. Chhabra, R.V. Jensen, Direct determination of the f(α) singularity spectrum, Phys. Rev. Lett. 62 (1989) 1327–1330.
[70] C. Lee, J. Brechtl, P.K. Liaw, Research on bulk-metallic glasses and high-entropy alloys in Peter K. Liaw's group and with his colleagues, Metallurgical and Materials Transactions A. 52 (2021) 2033–2093.
[71] M.A. Lebyodkin, D.A. Zhemchuzhnikova, T.A. Lebedkina, E.C. Aifantis, Kinematics of formation and cessation of type B deformation bands during the Portevin-Le Chatelier effect in an AlMg alloy, Results in Physics. 12 (2019) 867–869.
[72] L. Casarotto, H. Dierke, R. Tutsch, H. Neuhäuser, On nucleation and propagation of PLC bands in an Al–3Mg alloy, Materials Science and Engineering: A. 527 (2009) 132–140.
[73] A. Sarkar, P. Barat, P. Mukherjee, Multiscale entropy analysis of the Portevin-Le Chatelier effect in an Al-2.5%Mg alloy, Fractals. 18 (2010) 319–325.
[74] J. Brechtl, X. Xie, P.K. Liaw, S.J. Zinkle, Complexity modeling and analysis of chaos and other fluctuating phenomena, Chaos, Solitons & Fractals. 116 (2018) 166–175.
[75] E. Santos, M. Khosravy, M.A.A. Lima, A.S. Cerqueira, C.A. Duque, A. Yona, High accuracy power quality evaluation under a colored noisy condition by filter bank ESPRIT, Electronics. 8 (2019).
[76] M. Costa, A.L. Goldberger, C.-K. Peng, Multiscale Entropy Analysis of Complex Physiologic Time Series, Phys. Rev. Lett. 89 (2002) 068102.
[77] M.A. Lebyodkin, N.P. Kobelev, Y. Bougherira, D. Entemeyer, C. Fressengeas, V.S. Gornakov, T.A. Lebedkina, I.V. Shashkov, On the similarity of plastic flow processes during smooth and jerky flow: Statistical analysis, Acta Materialia. 60 (2012) 3729–3740.
[78] T.A. Lebedkina, M.A. Lebyodkin, Effect of deformation geometry on the intermittent plastic flow associated with the Portevin–Le Chatelier effect, Acta Materialia. 56 (2008) 5567–5574.
[79] Z. Lei, Y. Wu, J. He, X. Liu, H. Wang, S. Jiang, L. Gu, Q. Zhang, B. Gault, D. Raabe, Z . Lu, Snoek-type damping performance in strong and ductile high-entropy alloys, Science Advances. 6 (2020) eaba7802.
[80] M.A. Lebyodkin, T.A. Lebedkina, Multifractality and randomness in the unstable plastic flow near the lower strain-rate boundary of instability, Phys. Rev. E. 77 (2008) 026111.
[81] M.A. Lebyodkin, Y. Estrin, Multifractal analysis of the Portevin–Le Chatelier effect: General approach and application to AlMg and AlMg/Al_2O_3 alloys, Acta Materialia. 53 (2005) 3403–3413.
[82] J.F. Nye, Some geometrical relations in dislocated crystals, Acta Metallurgica. 1 (1953) 153–162.

[83] W. Pantleon, Resolving the geometrically necessary dislocation content by conventional electron backscattering diffraction, Scripta Materialia. 58 (2008) 994–997.
[84] B. Beausir, J.J. Fundenberger, Analysis Tools for Electron and X-ray diffraction, ATEX-Software, www.Atex-Software. Eu, Université de Lorraine-Metz, France (2017).

Figures

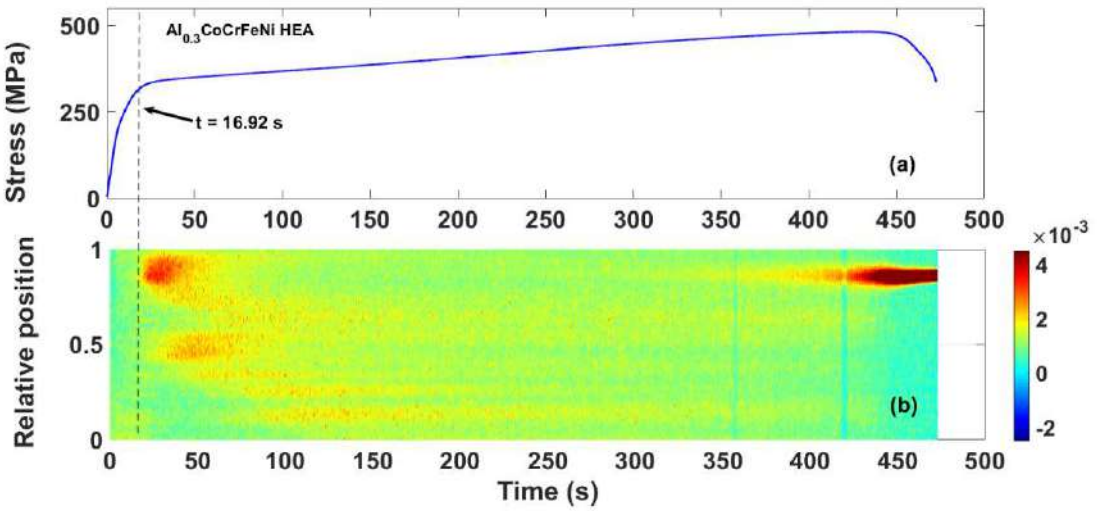

Fig. 1. An example of a deformation curve and the corresponding spatiotemporal map. (a) The stress vs. time data for the sample deformed at a strain rate of 10^{-3} s^{-1} and (b) the DIC map (the y-axis represents the position along the tensile axis in proportion to the gauge length). The dashed line corersponding to t = 16.92 s separates the region of a relatively-uniform plastic flow before the macroscopic elastoplastic transition.

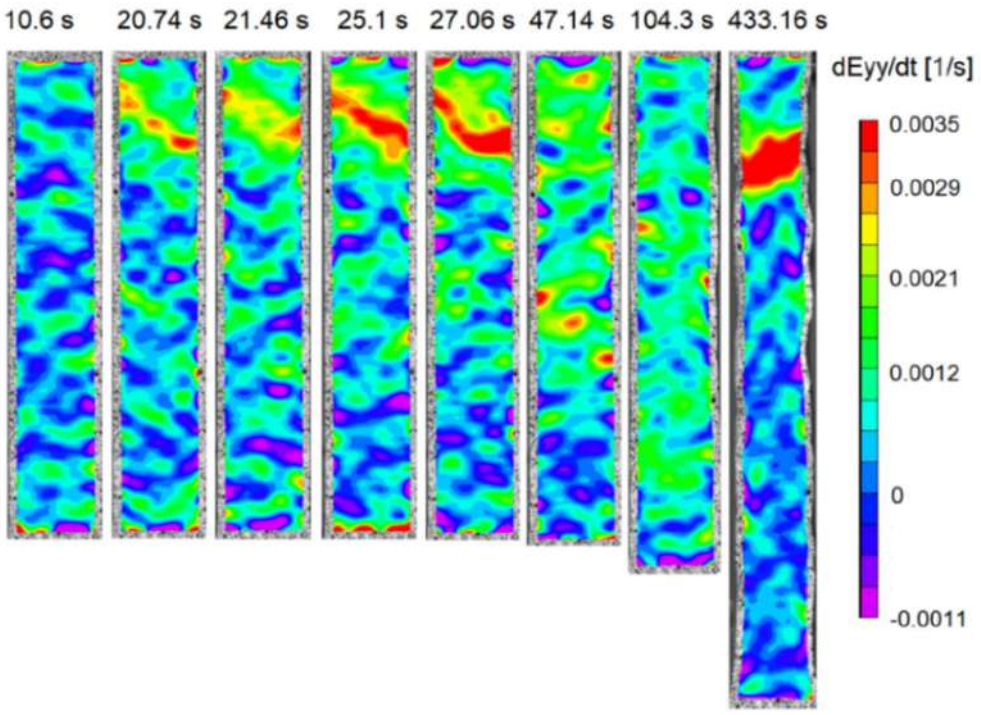

Fig. 2. The DIC for the $Al_{0.3}CoCrFeNi$ HEA sample of Fig. 1. Images of the local strain-rate field are superposed onto the photographs of the gauge part of the surface of the deforming sample, covered with a speckle pattern. It is worth noting the waviness of the borders of the heavily-deformed specimen in the last image. Green regions correspond to the strain rate around $\dot{\varepsilon}_a$.

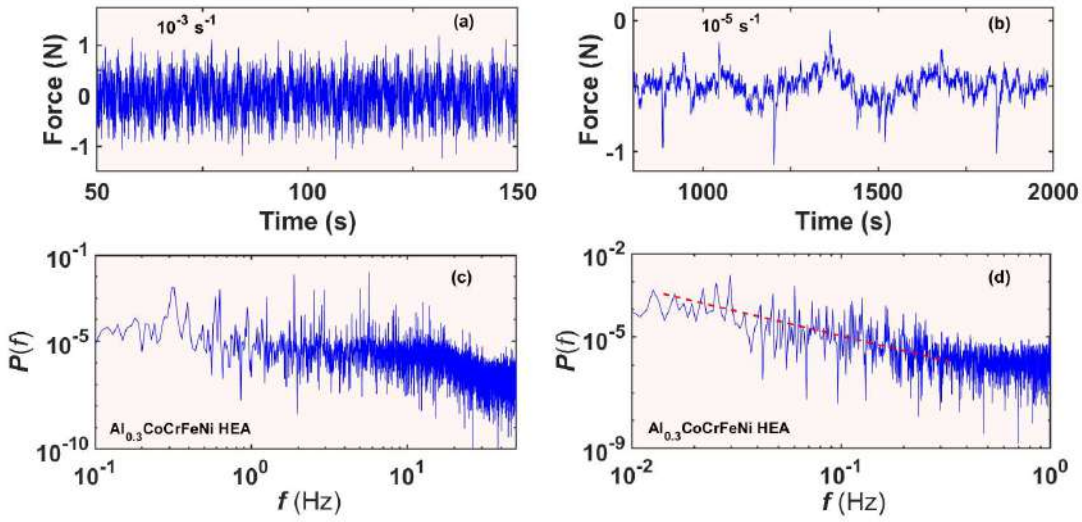

Fig. 3. Examples of the force response: detrended force vs. time signals for the samples tested at a strain rate of (a) 10^{-3} s^{-1} and (b) 10^{-5} s^{-1} and the corresponding power spectra (c) and (d). The dashed line in (d) traces $P(f) \sim 1/f^{1.8}$.

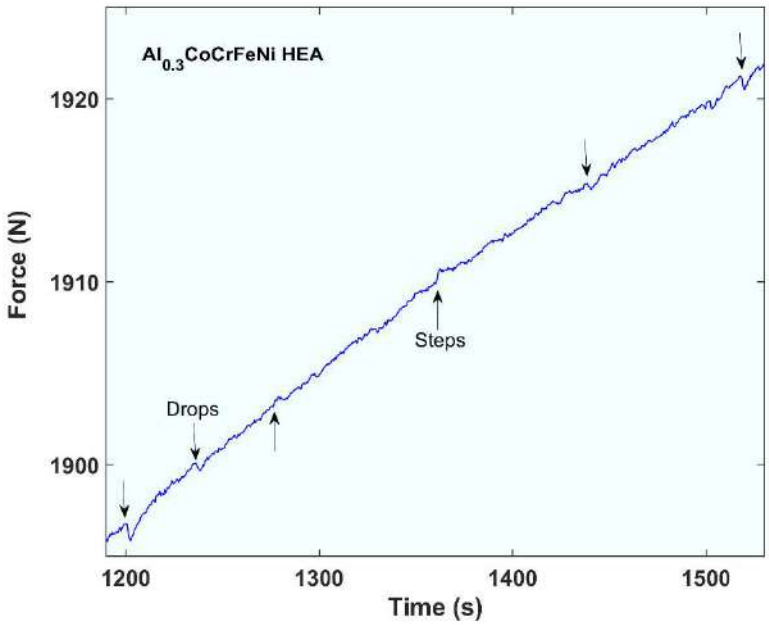

Fig. 4. The magnification of the raw *F(t)*-curve in a shorter time interval for the sample tested at a strain rate of 10^{-5} s^{-1}. Here, upward facing arrows indicate steps while downward facing arrows indicate drops.

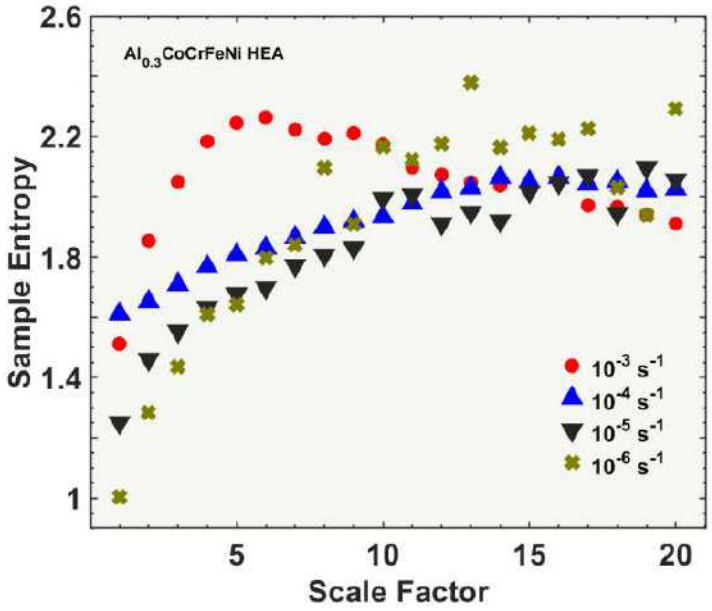

Fig. 5. RCMSE analysis of the force responses: the sample-entropy curves for the detrended force signals for $\dot{\varepsilon}_a$ ranging from 10^{-6} s^{-1} to 10^{-3} s^{-1}.

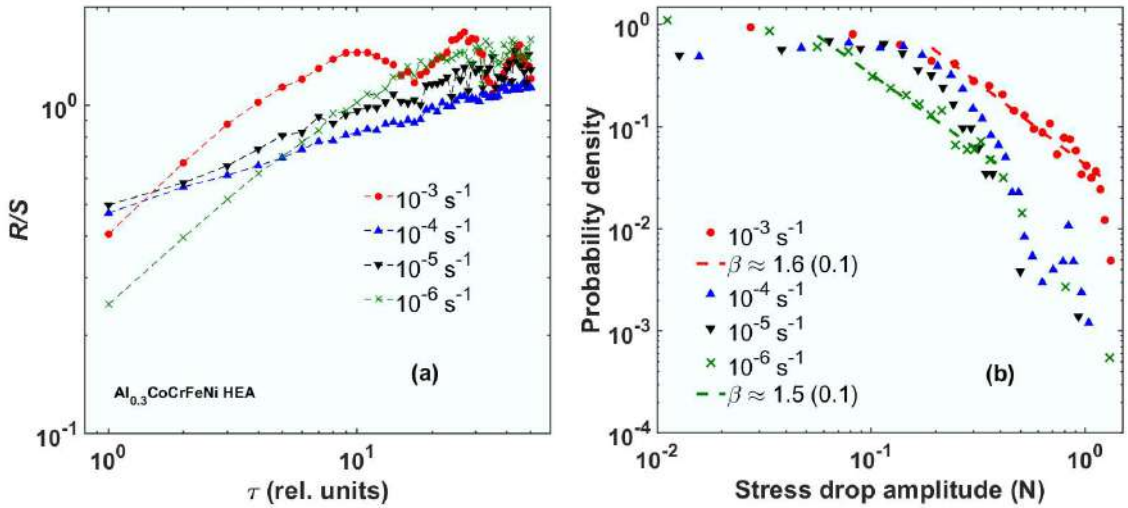

Fig. 6. Rescaled range and statistical analyses for the detrended force signals. (a) Log-log plots for the dependences of the rescaled R/S range on the time interval, τ, and (b) Probability distribution functions (PDFs) of the amplitude of fluctuations of the detrended force signals. The dashed lines in plot (b) trace power-law fits with the exponent, β, provided in the Figure legend for the corresponding PDFs.

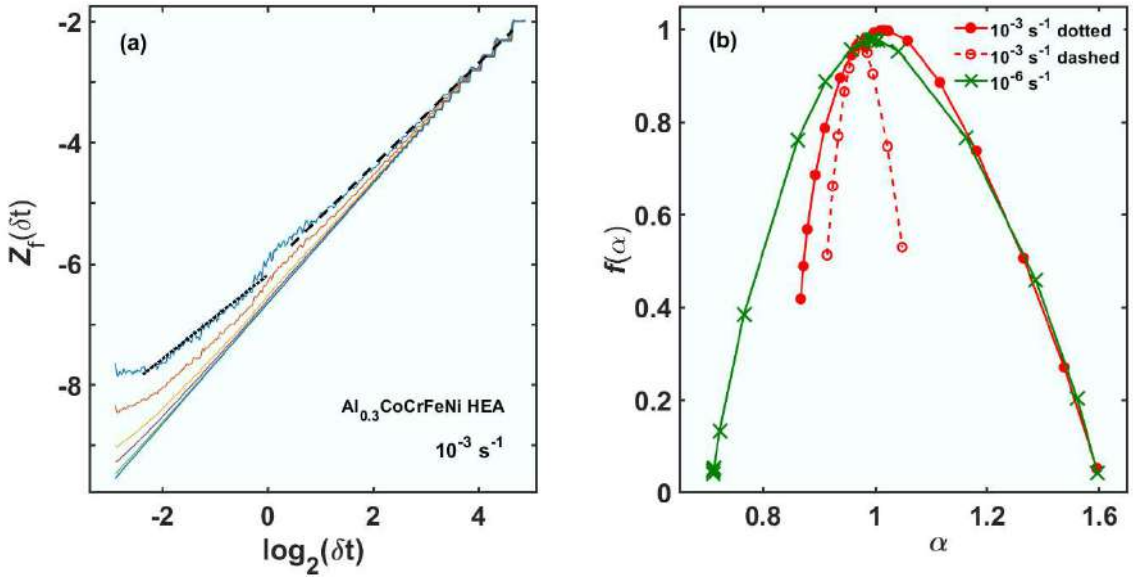

Fig. 7. Multifractal scaling for the force response. (a) Examples of the partition functions for the force signal corresponding to the sample tested at a strain rate of 10^{-3} s^{-1}; (b) the MF spectra for the intervals shown in chart (a) by the dotted and dashed lines (respectively, solid and open circles), as well as for the strain rate of 10^{-6} s^{-1} (crosses).

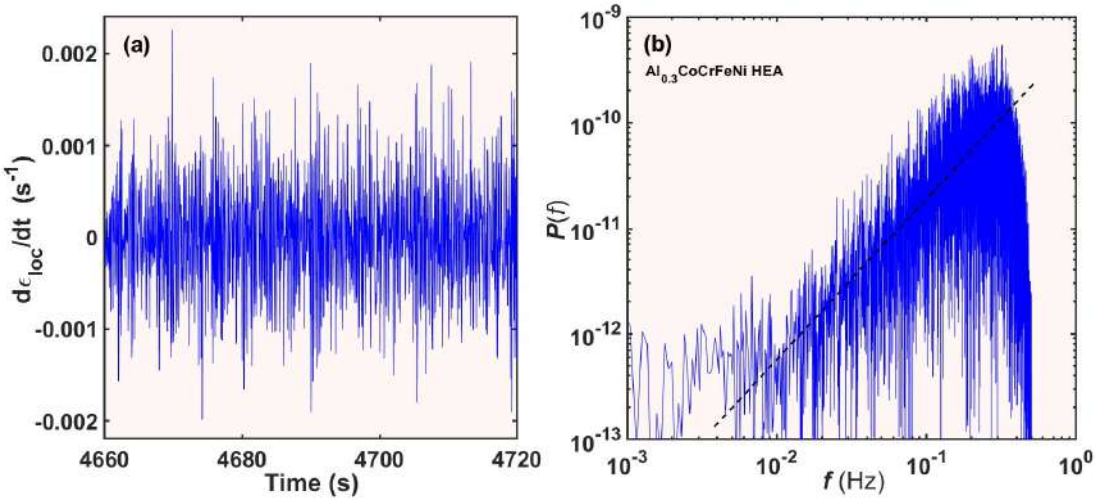

Fig. 8. Example of the local strain-rate response. (a) The detrended signal for the local $d\varepsilon_{loc}/dt$ signal corresponding to the middle of the gauge part of the sample tested at a strain rate of 10^{-5} s^{-1} and (b) its power spectrum (cf. Fig. 3). The dashed line corresponds to the function of $P(f) \sim f^{1.5}$.

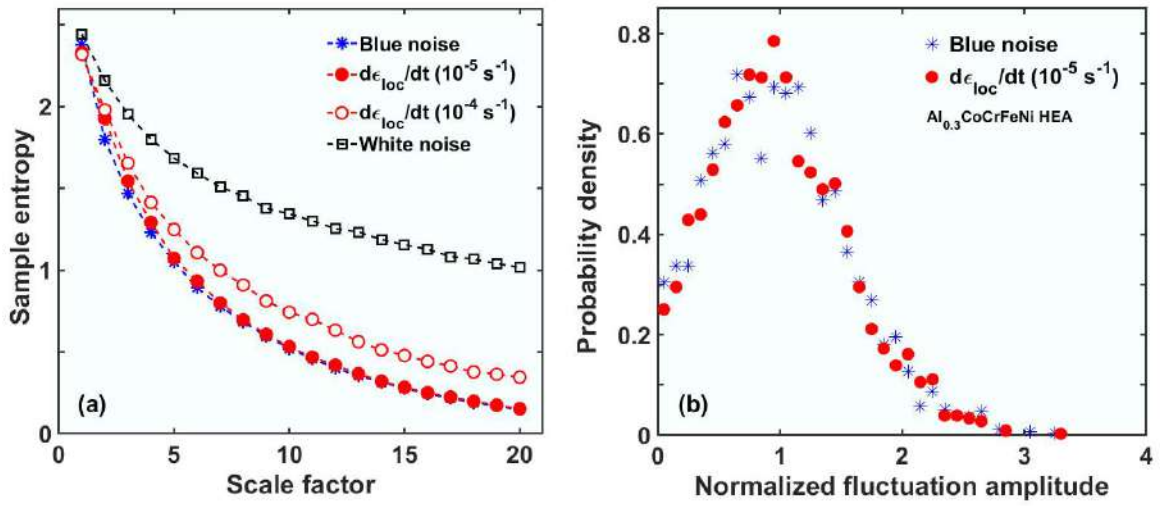

Fig. 9. Comparison of the RCMSE and statistical analysis results for the derivative of the local strain and colored noise. (a) The sample entropy vs. scale factor for the blue noise (blue stars), white noise (black squares), and the time derivative of the local strain for the samples tested at strain rates of 10^{-4} s^{-1} and 10^{-5} s^{-1} (respectively, open and solid red circles). (b) Semi-log plot of the PDF for the normalized fluctuation amplitudes for the blue noise and the local strain-rate signal recorded at 10^{-5} s^{-1}. The designations are the same as in chart (a).

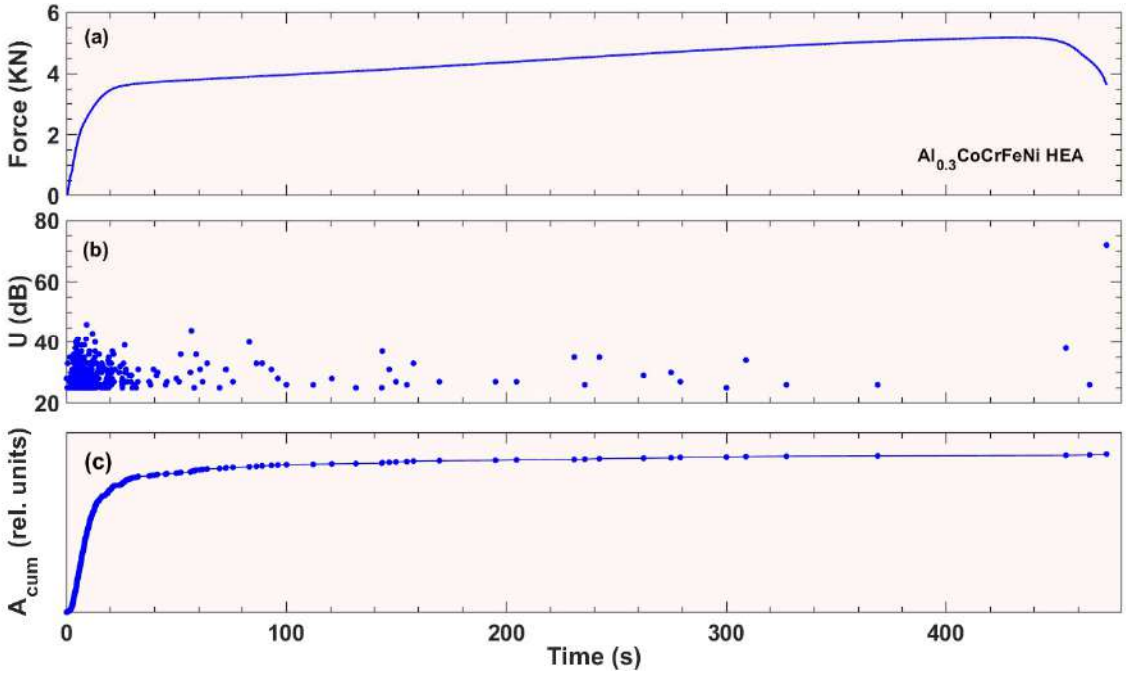

Fig. 10. Example of synchronization of the AE data with the deformation curve. (a) The time-dependent force for a sample tested at a strain rate of 10^{-3} s^{-1}, (b) the logarithmic amplitude, U, of the individual AE hits, and (c) the cumulated amplitude, A_{cum}, in linear units.

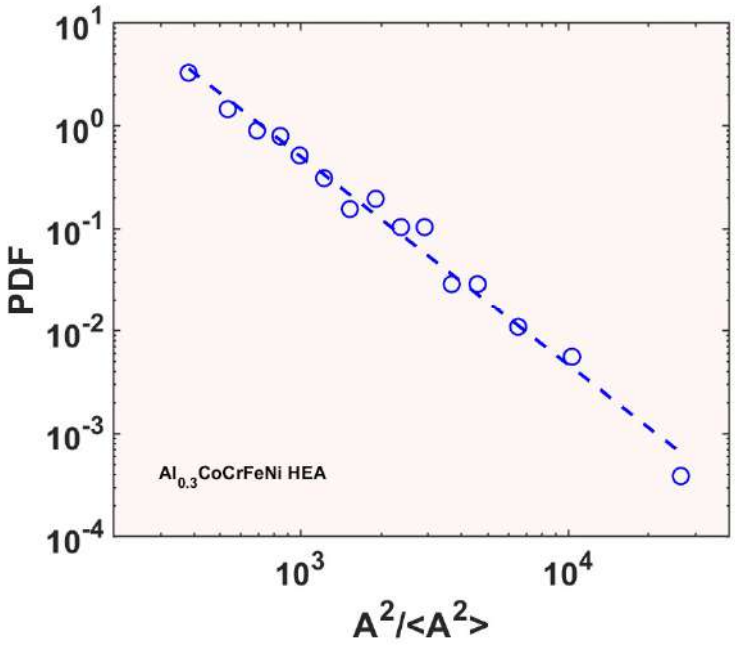

Fig. 11. Power-law statistics of the AE. The log-log plot of the PDF for the normalized intensity of the AE, $A^2/\langle A^2\rangle$, for a sample tested at 10^{-3} s^{-1}. The analyzed dataset contained 392 hits. The dashed line corresponds to an exponent, $\beta = 2.1 \pm 0.1$.

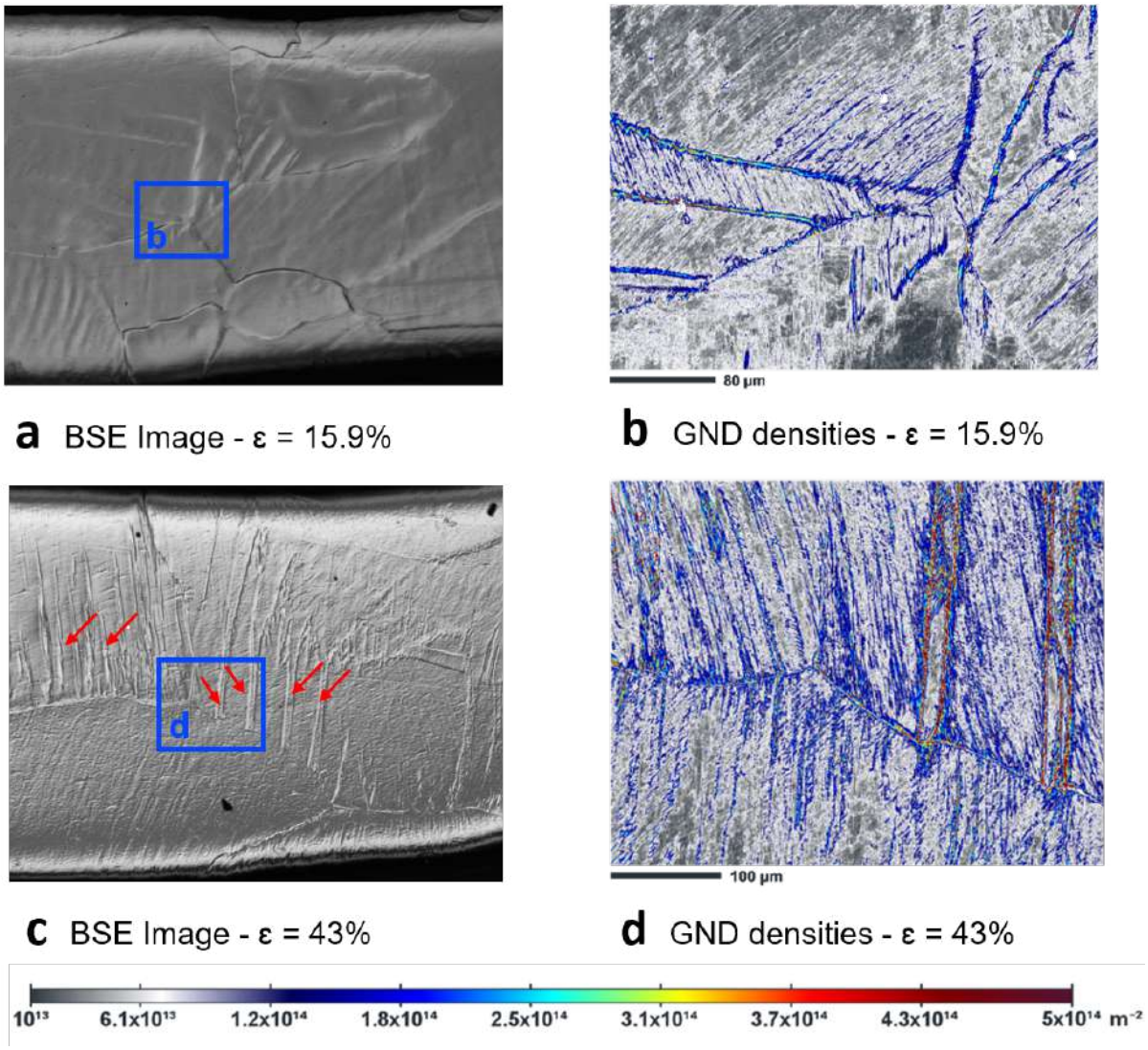

Fig. A1. Microstructures of the HEA samples deformed to strains of 15.9% and 43.3%. (a) and (c) - optical images. (b) and (d) - geometrically necessary dislocation (GND) densities for smaller regions approximately indicated on optical images. The grain boundaries in GND maps appear as black solid lines. Arrows indicate some of the twins presented in the microstructure.

Tables

Table 1. The complexity index and Hurst exponent (*CI* and *H*, respectively) for the force signals for $\dot{\varepsilon}_a$ ranging from 10^{-6} to 10^{-3} s^{-1}.

Strain Rate (s^{-1})	***CI***	***H***
10^{-3}	2.0696	-
10^{-4}	1.9218	0.22
10^{-5}	1.8441	0.27
10^{-6}	1.9406	0.65